Lawrence Berkeley National Laboratory
LBL Publications

Title
A unified catalytic mechanism in bifunctional DNA glycosylases with an evolutionarily conserved aspartate-lysine dyad

Permalink
https://escholarship.org/uc/item/61r7w8x3

Journal
Nature Communications, 17(1)

ISSN
2041-1723

Authors
Syed, A
Serafim, LF
Arvai, AS
et al.

Publication Date
2026-12-01

DOI
10.1038/s41467-026-75471-1

Copyright Information
This work is made available under the terms of a Creative Commons Attribution License, available at https://creativecommons.org/licenses/by/4.0/

Peer reviewed

eScholarship.org Powered by the California Digital Library
University of California

nature communications

Article

https://doi.org/10.1038/s41467-026-75471-1

A unified catalytic mechanism in bifunctional DNA glycosylases with an evolutionarily conserved aspartate-lysine dyad

Received: 28 May 2025

Accepted: 1 July 2026

Published online: 15 July 2026

Check for updates

Aleem Syed[1,2,12] ✉, Leonardo F. Serafim[3,12], Andrew S. Arvai[4], Irina G. Minko[5], Henry Y. H. Tang[1], Joy L. Huffman[4], Clifford D. Mol[4,13], Kenichi Hitomi[4,6,14], Altaf H. Sarker[7], Sudip Parikh[4], Chi-Lin Tsai[1], Albino Bacolla[1], David S. Shin[4], Richard P. Cunningham[8], Shigenori Iwai[6,9], Dipanjan Chowdhury[2], R. Stephen Lloyd[5,10], Ivaylo Ivanov[3] ✉ & John A. Tainer[1,4,11] ✉

Bifunctional glycosylases, OGG1 for purines and NTH1 for pyrimidines, repair oxidized DNA bases via consecutive glycosylase and AP-lyase reactions, yet their catalytic relationships and lyase activity's biological relevance remain unresolved. Here, we solved crystal structures of archaeal and human Ogg1 and Nth1 captured in key damage-recognition and catalysis-ready states, complemented by ab initio molecular dynamics simulations of their complete reaction trajectories. We thereby define a unified catalytic mechanism for OGG1 and NTH1 conserved over three billion years, distinct from the canonical oxocarbenium-ion mechanism of monofunctional glycosylases. While divergent in their oxidized substrate recognition, their chemistry converged on ribose protonation and ring opening that precede the deglycosylation step. Acid-base catalysis mediated by a conserved aspartate-lysine dyad lowers the C–N bond cleavage barrier, while the excised 8-oxoG base in OGG1 or a conserved aspartate in NTH1 facilitates the AP-lyase reaction. Moreover, structures of human OGG1 bound to product DNA and to product DNA plus a potent small-molecule agonist F51, within the catalytic pocket, reveal that agonists accelerate enzyme turnover by promoting product release. Together, these findings clarify the catalytic logic of bifunctional glycosylases, enabling the development of chemical tools to interrogate lyase activity and therapeutics for oxidative damage in cancer and aging.

High levels of damage to purine and pyrimidine bases arising from cellular metabolism and exogenous agents pose a major threat to genetic integrity[1–4]. To counter this threat, all domains of life rely on the evolutionarily conserved base excision repair (BER) pathway[5]. BER enzymes remove damaged (oxidized or alkylated) or inappropriate bases, such as uracil arising from misincorporation or cytosine deamination[3,6]. Since these BER enzymes are conserved from microbes to humans[7–9], insights into their fundamental mechanisms benefit from comparative structural and mechanistic analyses.

BER is initiated by DNA glycosylases through a nucleotide-flipping mechanism that extrudes damaged bases from the DNA double helix into the enzyme active site for recognition[10,11]. Oxidized DNA base lesions are typically excised by bifunctional glycosylase/lyases: glycosylase activity generates an AP (apurinic/apyrimidinic) site that is then

A full list of affiliations appears at the end of the paper. ✉e-mail: aleem_syed@dfci.harvard.edu; iivanov@gsu.edu; jtainer@mdanderson.org

incised by AP-lyase activity via either β−elimination, leaving a 3′-phospho−α,β−unsaturated aldehyde (3′-PUA) or β,δ−elimination, leaving a 3′-phosphate[12]. Following further processing of these 3′ modifications by apurinic/apyrimidinic endonuclease (APE1) or polynucleotide kinase-phosphatase (PNKP), respectively, templated resynthesis by either DNA polymerase β or δ replaces the missing nucleotides, and DNA ligase I or III seals the nicked DNA to complete BER[13,14].

Oxidation of purine or pyrimidine bases, arising from endogenous metabolism, is exacerbated by oxidative stress, inflammation, radiation, smoking, and environmental toxins such as arsenic[15–17], and generates diverse lesions[18,19]. Hydroxyl radicals can add to the C5-C6 double bond of thymine, producing thymine glycol (Tg). The resulting saturated pyrimidine loses ring planarity and has been shown to block repair and replicative polymerases in vitro[20–24]. Hydroxyl radicals can also add to guanine C4, C5, or C8 positions[25]. The C8-OH• adducts convert to the major stable product, 8-oxo-Guanine (8-oxoG), which can mispair with adenine via its Hoogsteen face, leading to GC→TA transversion mutations upon replication[26,27]. Most bifunctional purine/pyrimidine DNA glycosylases that catalyze β−elimination reactions belong to the helix-hairpin-helix (HhH) structural family[7–9]. Prominent members include endonuclease III-like protein 1 (NTH1), which excises oxidized pyrimidine lesions such as Tg, and 8-oxoG DNA glycosylase (OGG1), which excises the prevalent oxidized purine lesions (8-oxoG) from the genome[28–37].

The first DNA glycosylase crystal structure, solved over 30 years ago, was that of the bacterial glycosylase/lyase NTH (also known as endonuclease III)[33]; yet its lesion recognition and reaction mechanism have remained elusive until now. A structure-based general reaction pathway for bifunctional purine/pyrimidine DNA glycosylase/lyases[31,35] has been inferred largely from OGG1 studies[38–43], which implied a cofactor role for excised base using 8-oxoG analogs[44,45], plus comparative structural analyses of NEIL1–3 that belong to the helix-two-turn-helix (H2TH) family[46–49]. An intriguing study using a designer OGG1 double mutant K249C/C253K (which most likely altered the native mechanism) suggested analogy to monofunctional glycosylases, with direct nucleophilic attack on the glycosidic bond by an aspartic acid-activated water molecule[50]. Although NTH homologs share conserved catalytic residues and overall architecture with OGG1, their diverse substrate recognition pockets raise questions about mechanistic conservation[8]. Trapped intermediate structures and biochemical data from bacterial pyrimidine N-glycosylase/AP-lyases *Ec*Nth1 argue against product-assisted catalysis[35]. Furthermore, computational studies have focused primarily on the glycosylase step, leaving the AP-lyase reaction mechanism unresolved for both purine and pyrimidine bifunctional glycosylases. However, the biological relevance of the lyase activity is underscored by its improved contributions relative to APE1 for nucleosome-bound DNA[51]. Moreover, evidence for the importance of the DNA glycosylase/lyase activity for chromatin protection also comes from its damage surveillance of oxidation-susceptible sites to limit instability and cancer that likely originated ~500 million years ago during the buildup of free atmospheric oxygen[52].

Based on the evidence presented above, a key unanswered question therefore concerns the catalytic relationships connecting or separating the glycosylase and lyase chemical mechanisms. Monofunctional glycosylases, such as uracil DNA glycosylase[12,53], are thought to cleave the glycosidic bond via a stepwise mechanism that generates a high-energy, short-lived oxocarbenium intermediate or proceed via oxocarbenium-like predominantly dissociative transition states. In this scenario, the excision yields an anionic departing base (a poor leaving group) and a positively charged oxocarbenium cation, both necessitating strong electrostatic stabilization in the transition state. Early models for bifunctional glycosylases proposed that an amine (typically from a lysine or proline) activates water or directly attacks the oxocarbenium ion to form an iminium crosslink, after the base departs. More recent studies support a "ribose-protonated" mechanism specific to bifunctional enzymes[38,54–56]. In this mechanism, a neutral Lys attacks the ribose C1′, opening the deoxyribose ring between C1′ and O4′ prior to glycosidic bond scission, with ring opening requiring O4′ protonation by a catalytic aspartic acid; the glycosidic bond remains intact until the iminium crosslink is fully formed.

In this work, to elucidate how prototypical purine and pyrimidine glycosylase/lyase OGG1 and NTH1 enzymes recognize and remove damaged bases, including the relationship between glycosylase and lyase steps, we examined the structural and computational basis of their complete catalytic mechanisms. Leveraging evolutionary conservation, we determined crystal structures of *Archaeoglobus fulgidus* (*Af*) Ogg1 and Nth1 crystallized in key catalytic states. Using catalysis-ready intermediate crystal structures of *Af*Ogg1 bound to 8-oxoG and *Af*Nth1 bound to Tg substrates, combined with ab initio molecular dynamics (AIMD) and metadynamics (MTD) simulations in a QM/MM framework, we mapped both glycosylase and lyase reactions leading to the β−elimination product. Despite distinct damage recognition, our integrated analyses uncovered functional equivalences, analogous steps, and comparable energy barriers for the individual steps of purine and pyrimidine bifunctional catalysis carried out by OGG1 and NTH1, respectively. We also captured the β−elimination product (3′-PUA) in product-bound structures of *Af*Ogg1 and *Homo sapiens* (*Hs*) OGG1 crystal structures. Finally, by solving *Hs*OGG1 product-bound structures in the presence of small-molecule agonists, we show that agonists function by mimicking the excised base, thereby validating a product-assisted catalytic mechanism. Collectively, these results establish a unified understanding of OGG and NTH family bifunctional glycosylase/lyase catalysis with implications for developing chemical agonists and inhibitors.

Results

*Af*Ogg1 and *Af*Nth1 HhH enzymes as robust systems to characterize complete catalytic mechanisms of purine/pyrimidine bifunctional glycosylase/lyases

To elucidate the structural basis and optimum trajectory of the complete reaction mechanism for removal of oxidized purine and pyrimidine bases by bifunctional glycosylases, we utilized hyperthermophilic *Af*Ogg1 and *Af*Nth1 enzymes to trap multiple functional states. *Af*Ogg1 and *Af*Nth1 structures typify HhH superfamily DNA repair enzymes[7]. In both, the classical two-domain HhH fold, first identified in *Ec*Nth1[34], comprises a conserved six-helix barrel domain and a less-conserved four-helix bundle domain (Fig. 1a–d). They share characteristic structural motifs (canonical HhH[33], pseudo-HhH[57], and a gap-filling loop involved in substrate maneuvering) and key residues (for damaged-base recognition and catalysis) conserved in their human counterparts (Fig. 1a–d, Supplementary Fig. 1). These features make *Af*Ogg1 and *Af*Nth1 robust systems for dissecting the catalytic mechanism of purine/pyrimidine bifunctional glycosylases.

Beyond the core catalytic domains, *Af*Ogg1 contains N- and C-terminal extensions (Fig. 1a) distinct from the N-terminal domain in *Hs*OGG1 (Fig. 1b) or other HhH enzymes[7,31]. The *Af*Ogg1 N-terminus is compact, forming a long helix followed by an antiparallel β-sheet that pack against a short C-terminal extension inserted into the interface between the two core HhH domains (Fig. 1). This packing is stabilized by numerous hydrophobic residues within the unique *Af*Ogg1 terminus that interacts with the core HhH structure, exemplifying a tertiary structure whose primary role is to stabilize the buried C-terminus (Supplementary Fig. 2a). The buried C-terminal lysine (K198) is further stabilized by interactions of its main-chain carboxyl with H126, R129 and N130, and its side-chain amino group with E41 and Q60. This architecture contrasts with *Hs*OGG1, which has a large N-terminal domain that inserts a loop into the enzyme active site (Fig. 1b) and forms a hydrogen bond between the glycine backbone carbonyl in this loop and the protonated N7 of 8-oxoG[31].

https://doi.org/10.1038/s41467-026-75471-1

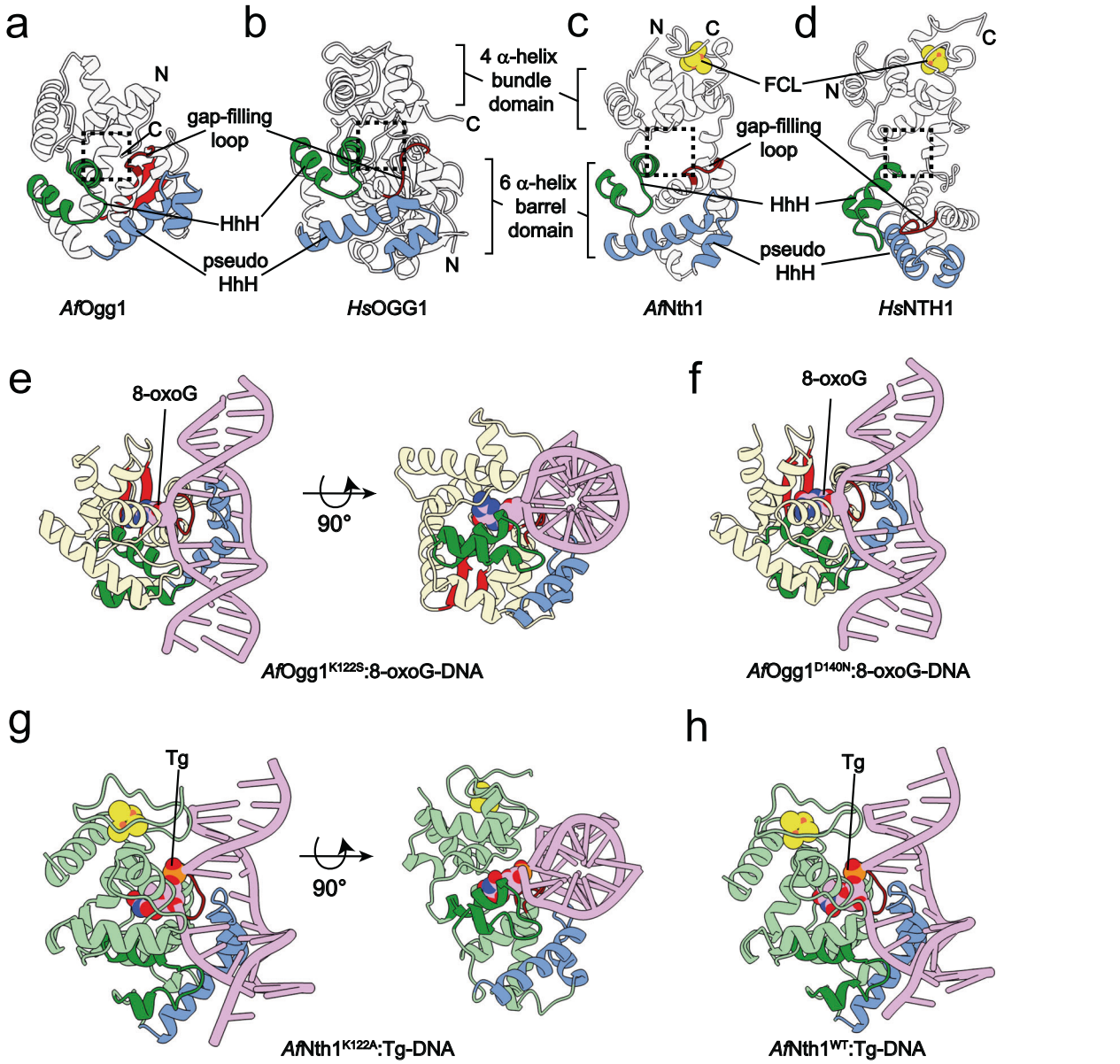

Fig. 1 | Conserved structural features of purine (OGG1) and pyrimidine (NTH1) bifunctional glycosylases. a Crystal structures of DNA-free *Af*Ogg1 (1.93 Å), showing the conserved four α-helix bundle domain, six α-helix barrel domain, helix-hairpin-helix (HhH) motif (shown in green), pseudo-HhH (shown in blue), and the gap-filling loop (shown in brown). The anti-parallel β sheets that pack against the C-terminal extension are shown in red. **b** Crystal structure of DNA-free *Hs*OGG1 (1.85 Å), **c** AlphaFold2-predicted model of DNA-free *Af*Nth1, and **d** Crystal structure of DNA-free *Hs*NTH1 (PDB: 7RDS[36]), featuring conserved structural folds and key motifs similar to *Af*Ogg1. Additionally, the NTH enzymes contain an iron-sulfur cluster (FCL, shown in spheres) in their C-terminus. Dashed squares represent the active site in each enzyme. **e** Crystal structure of *Af*Ogg1^{K122S} mutant bound to 8-oxoG-DNA substrate (2.5 Å), showing how each structural motif in *Af*Ogg1 engages DNA substrates in the intermediate state, and **f** Crystal structure of *Af*Ogg1^{D140N} mutant bound to 8-oxoG-DNA substrate (1.95 Å). The 8-oxoG lesion in the DNA is shown as spheres. **g** Crystal structure of Tg-DNA substrate bound to *Af*Nth1^{K122A} mutant (3.1 Å) and **h** Crystal structure of Tg-DNA substrate bound to *Af*Nth1^{WT} (3.5 Å), showing how each structural motif in *Af*Nth1 engages DNA substrates in the intermediate and pre-intermediate states, respectively. The Tg lesion is shown as spheres.

Among the two enzyme classes, the NTH bifunctional glycosylases that act on oxidized pyrimidine substrates are structurally less characterized, limiting comprehensive comparisons and unified mechanistic insights. Building on the first crystal structure of Nth1 from *E. coli* (*Ec*Nth1)[33], the AlphaFold2 (AF2)-predicted DNA-free and our Tg-DNA-bound *Af*Nth1 crystal structures show a similar HhH fold containing two core domains and a C-terminal 4Fe-4S cluster (FCL), as also seen in a recently solved DNA-free human NTHL1 (*Hs*NTH1) structure (Fig. 1c, d)[36]. In addition to these structural motifs that facilitate DNA binding, *Af*Nth1 and *Ec*Nth1 harbor a characteristic A-B loop connecting the two major domains, with a different length than *Hs*NTH1 (Fig. 1c, d and Supplementary Fig. 1b). Although this flexible loop is not resolved in the *Hs*NTH1 crystal structure, it enables *Hs*NTH1 to transition between the open and closed conformations essential for activity[36]. *Af*Nth1 also contains key conserved residues (e.g., K122 (K212 in *Hs*NTH1), D139 (D231), D46 (D136), H141 (H233), and N177 (N271)) that participate in catalysis and damaged-base binding in the active site. This conservation enabled us to crystallize *Af*Nth1 bound to Tg-containing DNA, providing structural insights into how the oxidized pyrimidine is recognized and bound in the Nth1 active site.

Lesion recognition and binding in *Af*Ogg1 and *Af*Nth1 co-crystal structures with their cognate substrates

To define lesion recognition and binding, we determined five informative crystal structures of *Af*Ogg1 and *Af*Nth1 with their respective cognate DNA substrates, capturing reaction intermediates. For *Af*Ogg1, we solved three structures: (i) two inactive mutants (K122S or D140N) bound to dsDNA containing a central 8-oxoG:C base pair (Fig. 1e, f and Supplementary Table 1), which adopt a similar global conformation (Supplementary Fig. 2b); and (ii) a WT selenomethionine (Se-Met) labeled DNA-free structure used for phasing in molecular replacement. *Af*Ogg1^{D140N} and *Af*Ogg1^{K122S} lack glycosylase activity, consistent with the captured intermediate structures. The K122S is assumed to be completely lyase deficient, given the key role it plays in the lyase reaction (the equivalent *Hs*OGG1^{K249Q} is shown to be inactive on an AP substrate[58]). In contrast, based on *Hs*OGG1^{D268N} data[59], *Af*Ogg1^{D140N} may retain partial lyase activity. For *Af*Nth1, we determined two *Af*Nth1-DNA complex structures: an inactive mutant (K122A) enzyme bound to a Tg:A-containing DNA substrate (Fig. 1g and Supplementary Table 2), and a WT-DNA complex crystallized at low temperature that captured a pre-intermediate state (Fig. 1h and Supplementary Table 2). The *Af*Nth1^{K122A} mutant is deficient for both glycosylase and lyase activity. In all intermediate or pre-intermediate complexes, the intact 8-oxoG or Tg nucleotide is flipped out of the DNA helix through the major groove and are bound within a damaged-base recognition pocket of the active sites in the *anti* configuration (Fig. 1e–h).

Double flipping of 8-oxoG and its opposite nucleotide in lesion recognition. A striking feature of the *Af*Ogg1^{D140N}-DNA complex is the double flipping of both the damaged nucleotide and its opposing nucleotide out of the DNA helix (Fig. 2a and Supplementary Fig. 2c). The resulting void is filled by residues from both the pseudo-HhH motif (R79 and F80) and the gap-filling loop (N50), stabilizing the DNA. This double-flipping may underlie the ability of *Af*Ogg1 to recognize and cleave 8-oxoG mispaired with adenine[60]. Although *Af*Ogg1 is less efficient on 8-oxoG:A than on 8-oxoG:C, the activity is substantial and appears to be unique to archaeal enzymes, as *Hs*OGG1 is inactive on 8-oxoG:A mispairs[31]. The lack of contacts with the opposite ("estranged") base likely contributes to *Af*Ogg1's reduced specificity for 8-oxoG:C, in contrast to *Hs*OGG1, which prefers C > T > G»A opposite to 8-oxoG due to R154 and R204 hydrogen bonds to cytosine N3 and O2 that cannot accommodate adenine[31]; accordingly, the R154H mutation yields a promutagenic enzyme that cleaves 8-oxoG opposite A as well as C[31]. The estranged cytosine in the *Af*Ogg1^{K122S} and *Af*Ogg1^{D140N} structures does not overlay well (Fig. 2a), and in *Af*Ogg1^{K122S}:DNA the estranged C forms two hydrogen bonds with R79, resembling *Hs*OGG1. Together, the two mutant structures reveal flexibility of the estranged base that facilitates its displacement from the double helix and may reflect an evolutionary relaxation of opposite-base specificity in *Af*Ogg1.

In the *Af*Ogg1-DNA structures, the enzyme makes multiple contacts with the damaged strand backbone, but almost none with the undamaged complementary strand (Fig. 2b), similar to *Hs*OGG1 and other glycosylases[31,61]. Recognition and cleavage of 8-oxoG base by both human and archaeal Ogg1 do not rely on specific contacts to the C8-O8 keto group; instead, a hydrogen bond forms between now-protonated N7 of the 8-oxoG and a conserved acceptor (Fig. 2c). In *Hs*OGG1, this acceptor is the backbone carbonyl oxygen of G42 in the N-terminal loop[31], whereas in *Af*Ogg1, it is the C-terminal carboxyl of K198, which participates in a charged triad (COO^-–R129–D185) engaging N7, O6, N1, and N2 of 8-oxoG. The C-terminal carboxylate, stabilized by H126 and a charge-neutralizing interaction between K198 and E41, reinforces the catalytic role of this buried residue.

Additional key interactions with 8-oxoG are mediated by W189, which stacks with the base, and H142, which forms a hydrogen bond with the 5′-phosphate. Relative to DNA-free *Af*Ogg1, these residues undergo substantial rearrangement to form the 8-oxoG binding pocket (Fig. 2d). H142 is conserved in *Hs*OGG1, whereas W189 is replaced by F319, which provides similar π–π stacking. The concerted movement of this His-aromatic pair appears critical for 8-oxoG binding. The catalytic residue K122 also reorients towards the active site upon 8-oxoG binding, whereas D140, which hydrogen bonds to the ribose, undergoes minimal displacement between the DNA-free and DNA-bound states (Fig. 2d). In the *Af*Ogg1^{D140N}, K122 fails to reorient despite proper 8-oxoG binding, indicating that D140 may also promote repositioning of K122 to assemble a catalysis-ready active site in *Af*Ogg1.

Pre-intermediate and intermediate states and lesion recognition in AfNth1–TgDNA-bound structures. We determined two *Af*Nth1 structures in complex with Tg:A-containing DNA: a WT complex crystallized at low temperature capturing a pre-intermediate state, and a catalytically inactive *Af*Nth1^{K122A} complex representing an intermediate state (Fig. 1g, h). The two states align well outside the DNA-binding regions but display pronounced differences in the DNA and in DNA-interacting elements (Fig. 2e and Supplementary Fig. 3a, b). The pre-intermediate is more open, while the intermediate state is more compact. In the pre-intermediate state, the damaged nucleotide is flipped out, but not yet fully inserted in the active site, representing a pre-catalytic state.

In this pre-intermediate state, Tg is positioned at the mouth of the active site cleft between the two HhH core domains and makes direct, damage-specific interactions with the conserved D46, highlighting its critical role in discriminating damaged from undamaged bases (Supplementary Fig. 3c). The previously solved *Ec*Nth1 structures lacked a bound oxidized base[35], whereas Tg-bound structures of other glycosylases (e.g., NEIL1) show no direct Tg-specific interactions[24,47]. This has led to the hypothesis that Tg is recognized before it is bound in the active site[47], or through an indirect mechanism[55], unlike OGG1, which showed a direct damaged-base-specific interaction. Our *Af*Nth1 pre-intermediate structure instead reveals direct recognition of the modified C5-C6 of Tg by a pyrimidine glycosylase. Supporting this observation, mutation of the equivalent D136 in *Hs*NTH1 severely impaired Tg excision, confirming its role in lesion detection (Supplementary Fig. 4).

In the intermediate state, *Af*Nth1 flips Tg out of the helix and induces a kink in the DNA. The FCL, pseudo-HhH, and HhH motifs all contribute to localizing the kink at the lesion. The void created by nucleotide extrusion is filled by residues from the B-C (gap-filling) loop (R43) and pseudo-HhH loop (F83). R43 contacts the adenine opposite Tg via a water molecule, but the estranged adenine remains in the helix, unlike the fully flipped opposite base in *Af*Ogg1. Additionally, *Af*Nth1 makes extensive contacts with the backbone of both DNA strands (Fig. 2f). The pseudo-HhH and HhH motif form a "pincher" grasp on the DNA, as proposed for MutY[57]. Specifically, residues G118-S123 of the HhH motif engage with the DNA backbone 3′ to the lesion, while the FCL inserts into the minor groove 5′ to the lesion, and residues F83-V86 of the pseudo-HhH motif contact the undamaged complementary strand.

Our *Af*Nth^{K122A}-DNA intermediate structure provides a detailed view of how Tg is bound in the active site of pyrimidine bifunctional glycosylase. The flipped Tg interacts with the protein residues Y130 and N177 (Fig. 2g). Relative to the pre-intermediate state, the damaged strand shifts deeper into the pocket and Tg rotates to contact N177 (Fig. 2h). Specifically, N177 forms hydrogen bonds with Tg O2 and N3, while Y130 interacts with O4. N177 is conserved *in Hs*NTH1, and mutation of the equivalent residue (N271A) in *Hs*NTH1 resulted in ~3–7-fold reduced Tg excision, but did not affect the AP-site processing, indicating a specific role in Tg binding (Supplementary Fig. 4). Y130 is

https://doi.org/10.1038/s41467-026-75471-1

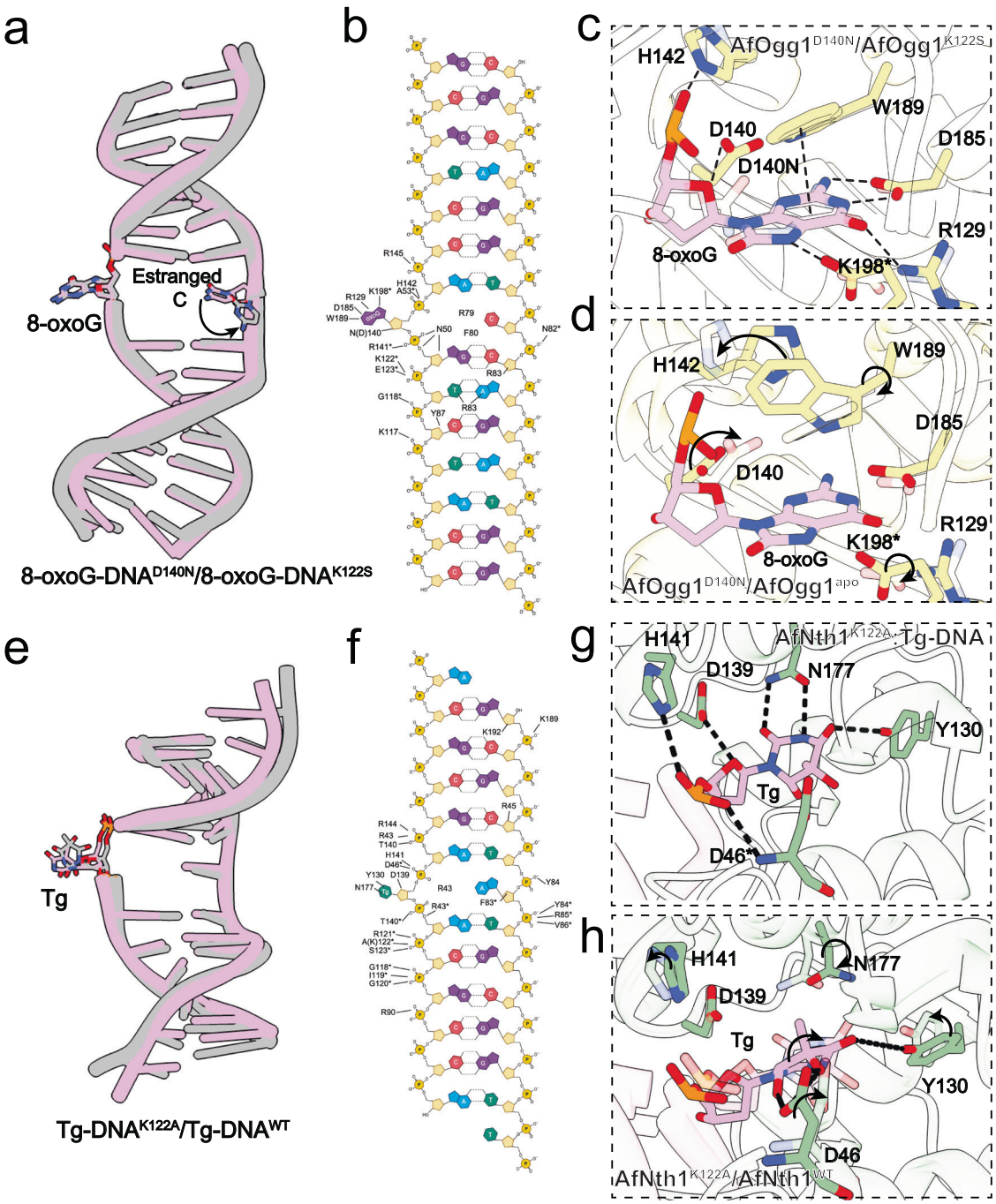

Fig. 2 | Protein-DNA interactions, lesion recognition and active site binding in *Af*Ogg1:8-oxoG-DNA and *Af*Nth1:Tg-DNA complexes. a Structural superposition of 8-oxoG-containing DNA substrates bound to *Af*Ogg1^{D140N}, (shown in grey) or *Af*Ogg1^{K122S} (shown in pink), showing the double nucleotide flipping of 8-oxoG and the estranged C. **b** Interaction network of protein-DNA interactions in the intermediate state of *Af*Ogg1^{D140N}:8-oxoG-DNA complex. Interactions between the DNA and protein main chain are indicated by an asterisk on the corresponding residues. Created in BioRender. Syed, A. (2026) https://BioRender.com/g23f502 **c** Interaction network showing how the 8-oxoG lesion is recognized in the superposed active site of *Af*Ogg1^{D140N} (residues shown in light yellow) and *Af*Ogg1^{K122S} (residues shown in yellow). Key residues interacting with the 8-oxoG lesion are highlighted. **d** Positional changes in the active site residues between superimposed DNA-free (shown in yellow) and DNA-bound state (shown in light yellow) as a result of 8-oxoG binding. **e** Structural superposition of Tg DNA substrates bound to *Af*Nth1^{K122A} (shown in pink) or *Af*Nth1^{WT} (shown in grey), indicating the differences between Tg binding in the intermediate and the pre-intermediate states, respectively. **f** Interaction network of protein-DNA interactions in the intermediate state of *Af*Nth1^{K122A}:Tg-DNA complex. Interaction between DNA and protein main chain is indicated by an asterisk on the corresponding residues. Created in BioRender. Syed, A. (2026) https://BioRender.com/k52y052 **g** Interaction network showing how the Tg lesion (shown in pink) is bound in the active site of the *Af*Nth1^{K122A} intermediate state. Key residues interacting with the Tg lesion are highlighted. **h** Changes in Tg lesion binding (shown with an arrow) and residues in the superimposed active site between pre-intermediate (Tg shown in pink and protein residues in green) and intermediate states (Tg shown in light pink and protein residues in light green). The Tg lesion discrimination by the D46 residue is also highlighted.

https://doi.org/10.1038/s41467-026-75471-1

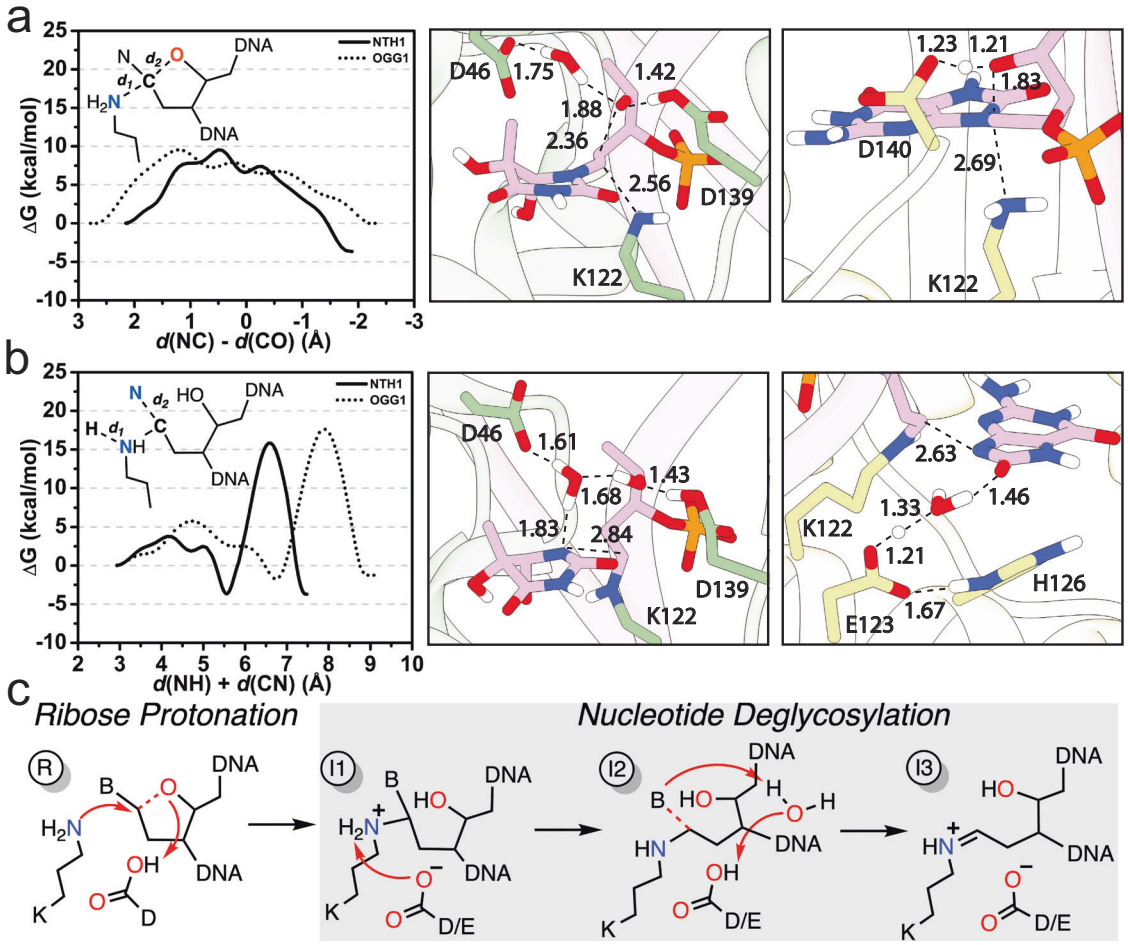

Fig. 3 | Mechanism of the glycosylase reaction performed by *Af*Nth1 and *Af*Ogg1. a, **b** The free energy profiles for the ribose protonation and nucleotide deglycosylation steps are shown in the left panels. A structural representation of the collective variables (CVs) used to create the MTD bias potential is shown in the insets (see also Supplementary Movies 1-4). Representative structures of the transition state associated with the rate-limiting step of each reaction are shown in the middle ($\mathbf{T1}^{Af\text{Nth1}}$ and $\mathbf{T3}^{Af\text{Nth1}}$) and right ($\mathbf{T1}^{Af\text{Ogg1}}$ and $\mathbf{T3}^{Af\text{Ogg1}}$) panels. **c** Overall reaction scheme depicting each elementary step of the glycosylase reaction, where R represents the reactant that includes the conserved Asp(D)-Lys (K) dyad, B stands for the damaged base, and reaction intermediates are labeled as I1, I2, and I3. The chemical bonds that are being broken during each step are shown as dashed bonds, and the flow of electrons is shown with red arrows.

not conserved; *Hs*NTH1 instead has V220 at the structurally equivalent position. In both *Af*Nth1 and *Hs*NTH1, the A-B loop caps the active site from the C5-C6 face of Tg. Given the longer, flexible A-B loop in *Hs*NTH1, we hypothesized that a loop residue might contact Tg O4 in the human enzyme. An AF3 model of *Hs*NTH1 bound to abasic dsDNA (since the Tg is not available in AF3), aligned with the $Af\text{Nth1}^{K122A}$ intermediate state structure, suggests that T107 from the A-B loop in *Hs*NTH1 may contact Tg O4 (Supplementary Fig. 4b). Consistent with the other glycosylase Tg-bound structures[24,47] and in our $Af\text{Nth1}^{K122A}$ intermediate structure, there are no direct protein contacts to the modified base; instead, conserved S41 interacts with the hydroxyl group at Tg C6 via a water molecule. Finally, as in *Af*Ogg1, conserved H141 contacts the 5′ phosphate of the lesion, and catalytic D139 hydrogen bonds with the ribose and likely steers K122 to assemble a catalysis-ready active site.

Complete reaction paths for purine/pyrimidine bifunctional N-glycosylases catalysis

By combining experimental structures of catalysis-ready intermediate states and AIMD, we simulated the complete reaction mechanism for N-glycosylase/AP-lyases featuring a conserved Asp–Lys catalytic dyad that excise a major class of oxidative purine (8-oxoG) or pyrimidine (Tg) lesions from genomic DNA.

Enzyme substrate complex. We first optimized the Michaelis complexes for *Af*Nth1 and *Af*Ogg1 by classical MD and QM/MM. Despite their common reactions, *Af*Nth1's active site is more solvent exposed, whereas the *Af*Ogg1 site contains the large hydrophobic residue W189 that provide π−π stacking and shield the 8-oxoG lesion from solvent. In both optimized Michaelis complexes, protonated aspartate, D139 in *Af*Nth1 or D140 in *Af*Ogg1, hydrogen bonds with the ribose oxygen of the lesion, positioning the catalytic Asp residue as the proton donor for the first activation step of the glycosylase reaction, consistent with other glycosylases[31,38,44,59,62]. Notably, $Af\text{Ogg1}^{D140N}$ fails to rotate the K122 side chain towards the active site, implicating D140 in both proton shuttling and positioning K122 for the nucleophilic attack.

Ribose protonation. The glycosylase reaction comprises two chemical events: (1) ribose ring opening and (2) base excision. Ribose opening occurs synchronously with ribose oxygen protonation by $D139^{Af\text{Nth1}}$ or $D140^{Af\text{Ogg1}}$, which initiates the glycosylase reaction. Ring opening proceeds as a concerted nucleophilic substitution, wherein the nucleophilic K122 of *Af*Nth1 (or *Af*Ogg1) attacks the C1′ carbon atom of the ribose ring, immediately after C1′-O4′ bond dissociation, through transition states $\mathbf{T1}^{Af\text{Nth1}}$ and $\mathbf{T1}^{Af\text{Ogg1}}$ with similar activation energies, ~10 kcal/mol (Fig. 3). Yet, the ribose oxygen atom in *Af*Nth1 can form an added water-mediated hydrogen bond with the D46 residue (Fig. 3a)

that facilitates cleavage of the scissile C1′-O4′ bond, thus promoting a more compact transition state compared to *Af*Ogg1. Consequently, the intermediate formed by *Af*Nth1 (**I1**$^{Af\text{Nth1}}$) after the reaction is about 4 kcal/mol more exergonic than the *Af*Ogg1 intermediate (**I1**$^{Af\text{Ogg1}}$).

To evaluate the possibility of direct glycosidic bond cleavage[54,63], we explicitly compared it against our proposed pathway involving ribose protonation first[54]. AIMD metadynamics simulations of both *Af*Nth1 and *Af*Ogg1 revealed that the direct glycolytic cleavage route consistently exhibits free energy barriers ~20 kcal/mol higher than the ribose ring-opening mechanism. Thus, base excision in both purine and pyrimidine bifunctional glycosylases requires initial ribose protonation and ring opening. Another widespread assumption in previous mechanistic work has been that the glycosylase reaction could proceed through the formation of a stable oxocarbenium intermediate[53]. In all our AIMD simulations, we failed to observe such intermediates. Moreover, starting from an oxocarbenium intermediate, we performed geometry optimizations using the same BLYP-D3 level of theory as the AIMD simulations. The resulting intermediate was >30 kcal/mol higher in energy than the respective enzyme-substrate complex (**R**$^{Af\text{Nth1}}$ or **R**$^{Af\text{Ogg1}}$), which effectively precludes discrete oxocarbenium ion involvement in catalysis. Instead, our computational analyses favor a mechanism in which the K122 amine group first attacks the deoxyribose ring and opens it between C1′ and O4′. The ring-opening step necessitates O4′ protonation. In this case, the glycosidic bond remains intact until the iminium crosslink is fully formed, and the ordering of catalytic events precludes discrete oxocarbenium ion formation. Unlike the canonical mechanism for monofunctional glycosylases where the base departs first, our mechanism for bifunctional glycosylases shows that ring-opening precedes base excision, thereby avoiding formation of a discrete, high-energy oxocarbenium intermediate.

Severing the glycosidic bond. Ring opening is followed by glycosidic C-N bond cleavage and formation of a Schiff base (**I3**). How enzymes facilitate the breakage of the exceptionally strong glycosidic bond has been a conundrum for the field of DNA repair. Strikingly, non-enzymatic C-N bond cleavage imposes a vast energetic penalty of ~30 kcal/mol[64]. There are multiple strategies that bifunctional glycosylases such as NTH1 and OGG1 may employ to lower this energetic penalty and achieve efficient catalysis. One strategy is the formation of a stable double bond (C=N) in the Schiff base, which is indeed the driving force of this chemical transformation. This process is achieved through deprotonation of K122. In the *Af*Nth1 enzyme, this is accomplished by D139 serving as a general base and by the carbonyl group (O2) of the Tg base. By contrast, in the *Af*Ogg1 enzyme, analogous proton transfer is mediated by an active site water molecule proximal to the general base E123. In both enzymes, the dissociation of the N-H bond involves comparable free energy barriers, ~4 kcal/mol for *Af*Nth1 and ~6 kcal/mol for *Af*Ogg1 (Fig. 3b). The resulting protonated Schiff base (**I2**) is exergonic in comparison with the respective ribose protonated intermediates (**I1**$^{Af\text{Nth1}}$ and **I1**$^{Af\text{Ogg1}}$) for both enzymes. Despite the overall unified mechanism, there are a few differences between the two enzymes. Due to the opposite orientations of the proton-abstracting residues in the two proteins, the newly formed C-N partial double bonds have distinct geometric isomerism. In *Af*Nth1, formation of a *trans* isomer is favored, in which the polar lysine hydrogen atom points away from D139. In *Af*Ogg1, the product is a *cis* isomer with the equivalent hydrogen atom oriented towards D140.

The next step is the dissociation of the glycosidic bond after the C-N bond to the lesioned base has been significantly weakened by (1) ribose ring opening; (2) proton shuttling; and (3) Schiff base partial C=N bond formation. Nonetheless, in both enzymes, C-N bond dissociation is the rate-limiting step of the glycosylase reaction, yielding free energy barriers of ~18.4 and ~18.9 kcal/mol for *Af*Nth1 and *Af*Ogg1, from their respective intermediates **I2** (Fig. 3b). In both systems, water molecules mediate protonation of the damaged bases, which additionally stabilizes the transition states. In *Af*Nth1, D46 participates in the proton transfer, which occurs at the N1 atom of the Tg base. Correspondingly, in *Af*Ogg1, E123 acts as the general acid protonating the O8 atom of the 8-oxoG base. Consistent with these roles, *Af*Ogg1 E123A and *Hs*NTH1 D136A (D46 equivalent) mutants are inactive on their respective substrates (Supplementary Fig. 4, 5).

Our computational analyses are support and extend previously reported comparable deglycosylation reaction rates for OGG1 and NTH1[36,50]. In both *Af*Nth1 and *Af*Ogg1, water molecules mediate protonation of the damaged base and contribute to the stabilization of both the transition state and the product complex. The overall deglycosylation reaction is thermodynamically more favorable in *Af*Nth1 (Supplementary Fig. 6, 7). This greater exergonicity arises primarily from differences in active-site solvation: the *Af*Nth1 active site is more solvent-exposed, allowing more water molecules to participate and form an extended hydrogen-bonding network that strongly stabilizes the open-ribose conformation and lowers the energy of intermediate **I1**$^{Af\text{Nth1}}$. In contrast, *Af*Ogg1 features a more enclosed active site with a hydrophobic residue (W189) shielding the base and limiting water access. This structural enclosure hinders escape of the excised 8-oxoG, trapping it in the active site. This both reduces solvation-driven stabilization and suppresses the entropic gain upon product release.

Schiff base hydrolysis. Similar to the glycosylase step, the AP-lyase activity of bifunctional glycosylases involves two separate chemical events: (1) Schiff base hydrolysis; and (2) β-elimination. In the first step, a water molecule carries out a nucleophilic attack onto the C1′ atom of the Schiff base. The negatively charged residues D46 and E123 (in *Af*Nth1 and *Af*Ogg1, respectively) abstract the proton from the water molecule to generate the nucleophilic hydroxyl ion (Fig. 4). This concerted step is associated with free energy barriers of ~7 kcal/mol for both enzymes (Fig. 4a). The carbinolamine (**I4**), which is endergonic with respect to the Schiff-base (**I3**), is generated as an intermediate after this step.

In the second step, the unstable carbinolamine intermediate collapses by a proton transfer promoted by residue D139 (D140 in *Af*Ogg1). The deprotonation event also triggers the dissociation of the C-N bond, which releases K122 from the newly formed aldehyde group at the end of the ribose (**I5**) (Fig. 4b). At this stage, the enzyme/DNA complex is held together only by intermolecular forces, which allows dissociation of the glycosylases from product DNA, a process often facilitated by downstream BER factors such as APE1[65,66].

β-elimination. The β-elimination step is the final chemical event of the AP-lyase reaction and the rate-limiting step of the entire bifunctional catalysis. This reaction occurs in one single step with the synchronous elimination of one of the H2′ hydrogen atoms of C2′ and the dissociation of the C3′-O3′ bond that connects the ribose and the phosphate group. Due to the opposite orientation of these chemical bonds in **I5**, two catalytic residues (general base and general acid) are necessary for the elimination to occur. In *Af*Nth1, we observe a water-mediated proton abstraction from C2′ to the D46 residue. Concurrently, D139 acts as a general acid, protonating the oxygen atom of the phosphate group and assisting its departure from the ribose. In *Af*Ogg1, the excised 8-oxoG can act as a general base in a water-mediated proton abstraction from C2′. Although E123 is the final proton acceptor, the 8-oxoG base serves as a cofactor facilitating the shuttling of the proton by lowering the energy of the transition state associated with the reaction. Excluding 8-oxoG from the simulation increases the free energy of this step by ~5 kcal/mol, confirming its catalytic contribution (Supplementary Fig. 8). Since E123 is not conserved in the human enzyme, we tested whether this key feature could be transplanted into *Hs*OGG1. However, both V250D and V250E mutants were inactive on 8-oxoG-DNA (Supplementary Fig. 9). This

https://doi.org/10.1038/s41467-026-75471-1

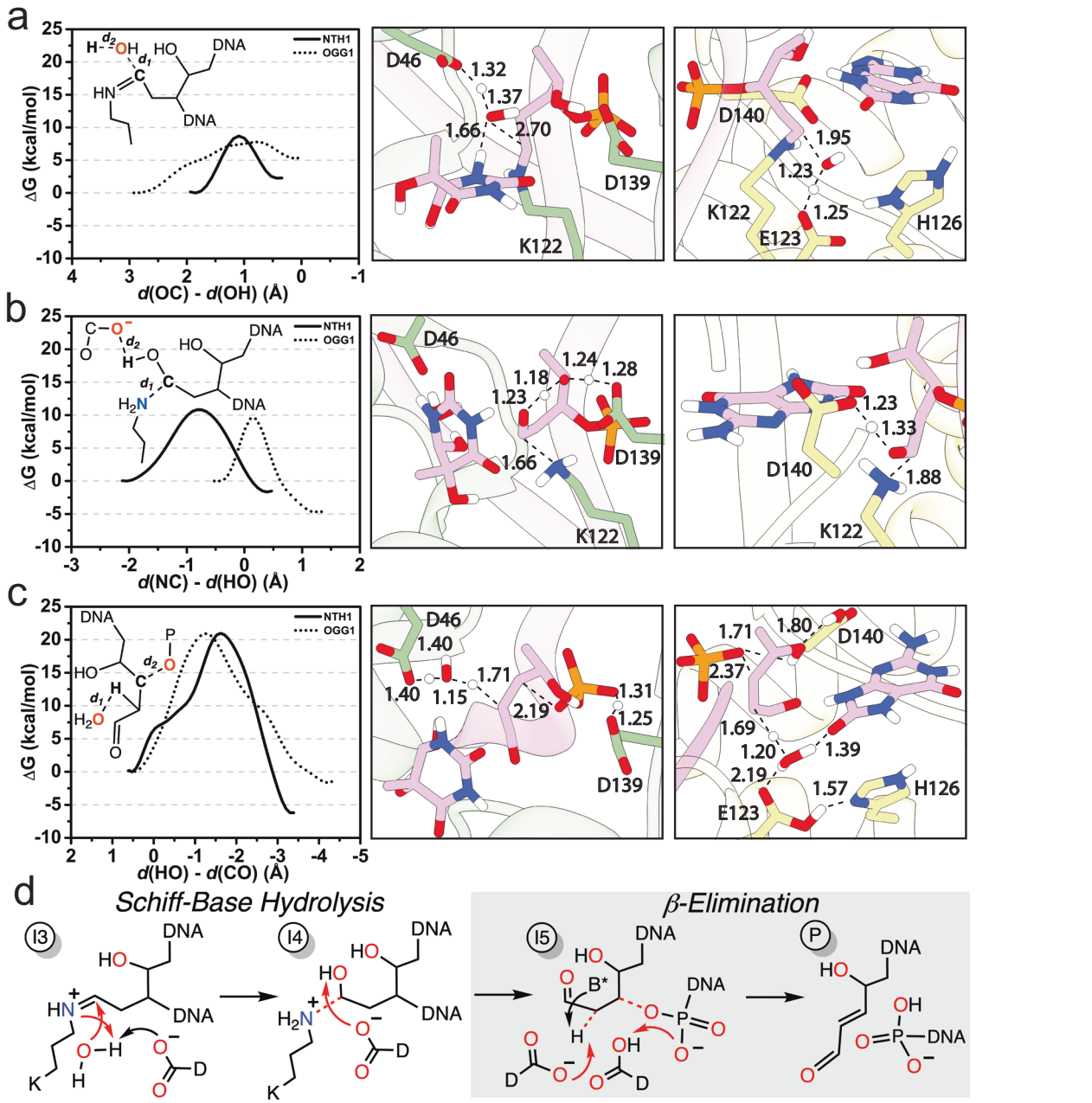

Fig. 4 | Mechanism of the AP-lyase reaction performed by *Af*Nth1 and *Af*Ogg1. **a**–**c** The free energy profiles for the Schiff base hydrolysis and β-elimination steps are shown in the left panels. A structural representation of the collective variables (CVs) used to create the MTD bias potential is shown in the insets (see also Supplementary movies 5–10). Representative structures of the transition state associated with the rate-limiting step of each reaction are shown in the middle (**T4**$^{Af/Nth1}$, **T5**$^{Af/Nth1}$ and **T6**$^{Af/Nth1}$) and right (**T4**$^{Af/Ogg1}$, **T5**$^{Af/Ogg1}$ and **T6**$^{Af/Ogg1}$) panels. **d** Overall reaction scheme depicting each elementary step of the AP-lyase process. In intermediates **I3, I4** and **I5**, black arrows denote fast protonation events catalyzing the reaction, whereas the red arrows indicate the flow of electrons. The chemical bonds that are being broken during each step are shown as dashed bonds.

underscores that, although archaeal and human enzymes share the same overall mechanism, additional non-conserved active-site features modulate catalysis and cannot be recapitulated by single-residue substitutions.

The dissociation of the C3′-O3′ bond is assisted by the protonated D140, which donates a proton to the negatively charged oxygen atom of the phosphate group. In both enzymes, this concerted step is associated with a free energy barrier of ~21 kcal/mol (Fig. 4c). The final product is the 3′-PUA, which is exergonic by about 10 kcal/mol with respect to **R**. In contrast to the glycosylase step, where both chemical events target the C1′ atom and their order strongly influences energetics, the AP-lyase step involves events at two separate sites (Schiff-base hydrolysis at C1′ and β-elimination at C3′). This separation allows flexibility in the sequence of chemical events; however, the much faster rate of hydrolysis ensures it precedes β-elimination in practice, with negligible impact on the overall energetics (Supplementary Fig. 10). The calculated energy barriers are consistent with the experimentally observed trends in reaction rates, within the systematic computational errors expected for DFT calculations: NTH1 processes Tg nominally ~6–10 times faster than OGG1 processes 8-oxoG in bifunctional glycosylase reaction (Supplementary Figs. 4, 8, 9). This is striking given the distinct chemistry of their departing nucleobases. The reason why similar rates arise despite dissimilar departing nucleobases is an intriguing question. Gas-phase QM studies of

https://doi.org/10.1038/s41467-026-75471-1

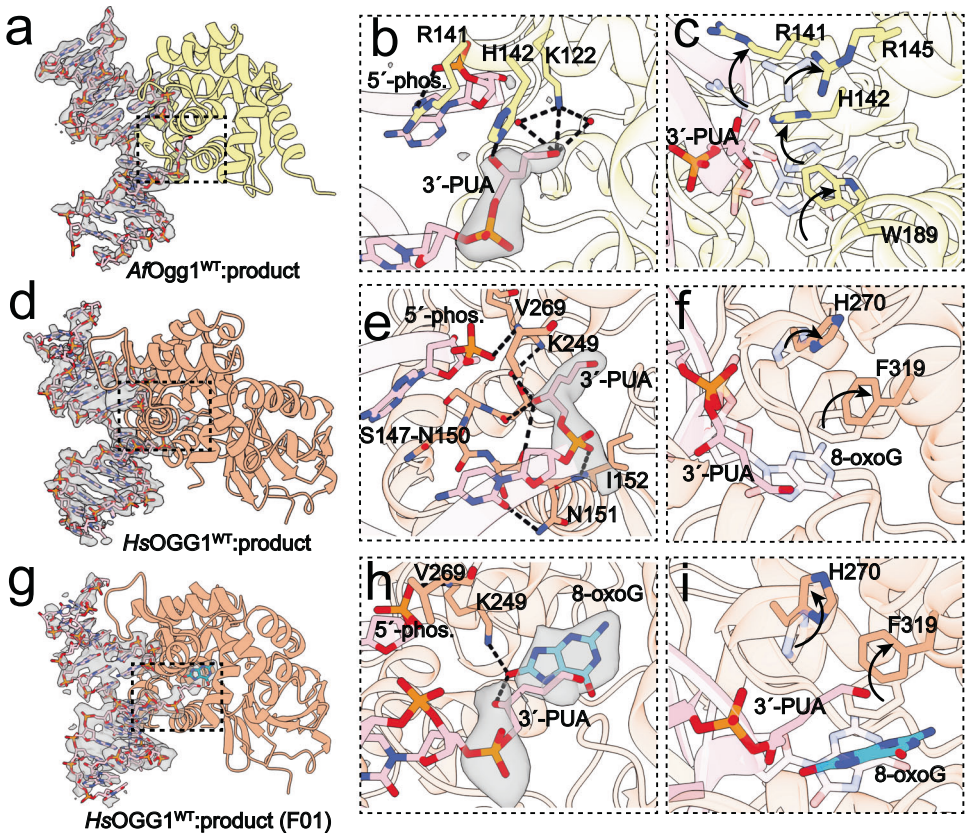

Fig. 5 | Product-bound OGG1 structures and their implications for OGG1 activation. a Crystal structure of product-bound *Af*Ogg1^{WT} (2.0 Å) with 2Fo-Fc simulated annealing (SA) composite omit map shown (in grey) for the bound DNA. The map is contoured at 1σ and carved at 2 Å. **b** The PHENIX polder omit map shown (in grey, contoured at 4σ) for the 3′-PUA product bound in the active site. Protein residues are shown in yellow and nucleobases, including the 3′-PUA, are shown in pink. **c** Positional changes in the active site residues (shown as sticks) between the superimposed intermediate (shown in light yellow for protein residues and in light pink for the nucleobases) and product-bound states (shown in yellow for protein residues and in pink for the nucleobases, including 3′-PUA) are highlighted by black arrows. **d** Crystal structure of product-bound *Hs*OGG1 (WT) (2.0 Å) with 2Fo-Fc SA composite omit map shown (in grey) for the bound DNA. The map is contoured at 1σ and carved at 2 Å. **e** The PHENIX polder omit map shown (in grey, contoured at 6.75σ) for the 3′-PUA product bound in the active site. Protein residues are shown in salmon and nucleobases, including the 3′-PUA, are shown in pink. **f** Positional changes in the active site residues (shown in sticks) between the superimposed intermediate (shown in light salmon for protein residues and in light pink for the nucleobases, PDB ID: 1EBM[31]) and product-bound states (shown in salmon for protein residues and in pink for the nucleobases, including 3′-PUA) are highlighted by black arrows. **g** Crystal structure of product-bound *Hs*OGG1 (WT) in the presence of agonist F01 (2.5 Å) with 2Fo-Fc SA composite omit map shown (in grey) for the bound DNA. The map is contoured at 1σ and carved at 2 Å. **h** The PHENIX polder omit maps (shown in grey) for the 3′-PUA product (contoured at 6σ) and the excised 8-oxoG base (contoured at 6.5σ) bound in the active site. **i** Positional changes in the active site residues (shown in sticks) between the superimposed intermediate (shown in light salmon for protein residues and in light pink for the nucleobases, PDB ID: 1EBM[31]) and the product bound in the presence of F01 ((shown in salmon for protein residues and in pink for the nucleobases). The flipped-out 8-oxoG lesion in the intermediate state (shown in light pink) and excised 8-oxoG in the product state are shown in cyan.

uncatalyzed glycosidic bond cleavage show substantial variability in activation barriers[67]. The study also revealed strong dependence on the protonation state, exact protonation site, and chemical modifications to the base, although differences were predicted to diminish in condensed phase or enzymatic environments. For 8-oxoG and Tg, uncatalyzed barriers are relatively similar (135.2 vs 143.8 kJ/mol; $\Delta\Delta G \approx 2.05$ kcal/mol). Thus, we cannot exclude that we selected substrates with similar intrinsic barriers. Nevertheless, the sensitivity of reaction rates to protonation and hydrogen bonding suggests glycosylases may have evolved to constrain cleavage rates within a narrow, physiologically relevant range. Therefore, it is indeed interesting to consider that NTH and OGG operate with vastly different efficiencies expressly to compensate for the intrinsic dissimilarity between purine and pyrimidine substrates.

Product-bound Ogg1 structures and agonist implications

Unsuccessful crystallization attempts implied that product-bound *Af*Nth1 is highly flexible, as we only obtained WT *Af*Nth1:Tg-DNA complex crystals at low temperature. These crystals captured a pre-intermediate state, despite the robust activity of AfNth1 on both Tg- and AP-site-containing DNA substrates (Supplementary Fig. 11). In contrast, we solved a WT *Af*Ogg1:8-oxoG-DNA co-crystal structure at 2 Å (Fig. 5a and Supplementary Table 1). The electron density shows that *Af*Ogg1 has cleaved and released the 8-oxoG, and the Schiff base has undergone β-elimination to generate a single-strand DNA break (Fig. 5a and Supplementary Fig. 12a). A PHENIX polder omit map reveals clear density for the 3′-PUA, while the excised base is absent and the active site is solvent-filled. The 3′-PUA interacts with water molecules and K122, and the 5′-phosphate is stabilized by R141 and water (Fig. 5b and Supplementary Fig 12a). Globally, the product-bound *Af*Ogg1 structures closely resemble the apo and intermediate structures (r.m.s.d. 0.53–0.55 Å), but the active site and DNA geometry differ: W189 returns to its DNA-free position, and H142 remains engaged with 3′-PUA. Additionally, fewer contacts are made to the sugar-phosphate backbone in the product-bound structure, as R141 and R145 move away from the DNA backbone, and cleaved DNA is more bent, consistent with increased flexibility (Fig. 5c).

We also obtained the WT *Hs*OGG1:8-oxoG-DNA product-bound structure at 2 Å (Fig. 5d and Supplementary Table 3). Strong density in the SA composite omit map confirms a product state in which *Hs*OGG1 cleaved 8-oxoG and catalyzed β-elimination, generating a ssDNA break (Fig. 5d and Supplementary Fig 12b). The 5′-phosphate is stabilized by V269 and a water-mediated contact with K249. Clear density for 3′-PUA in the polder omit map supports our computational and prior biochemical data. The 3′-PUA binding is stabilized by S147, N150, I152 and K249 (Fig. 5e). The overall protein fold resembles the 8-oxoG-bound intermediate state[31], but the active site is more open and similar to the DNA-free state: the H270-F319 pair reverts to its apo configuration, and no density is present for the excised 8-oxoG, indicating its release (Fig. 5f and Supplementary Fig. 12c).

Our QM/MM analyses indicate that excised 8-oxoG acts as a cofactor during the AP-lyase step of the *Af*Ogg1, supporting and extending previous observations[44]. This finding supports that OGG1 activity could be enhanced by small-molecule agonists with therapeutic potential in inflammation and aging[68–70]. To investigate this further, we co-crystallized WT *Hs*OGG1:DNA with agonist F01 (compound F in reference[68]), a proposed allosteric activator of *Hs*OGG1[70]. The 2.5 Å *Hs*OGG1:DNA + F01 structure resembles the product-bound state but, critically, exhibits clear density for 8-oxoG retained in the active site (Fig. 5g-h and Supplementary Table 3). The H270-F319 pair is disrupted, with F319 now contacting 8-oxoG, while H270 is displaced (Fig. 5i). Although F01 density is not observed, the presence of bound 8-oxoG in the active site and the accompanying subtle rearrangements support an allosteric *Hs*OGG1 activation, as mediated by the excised 8-oxoG in the active site. The 3′-PUA product has shifted to accommodate 8-oxoG (Supplementary Fig. 12d). This active-site flexibility suggests that a more potent agonist could replace the loosely bound 8-oxoG and further enhance enzymatic turnover. Consistent with this interpretation, five different *Hs*OGG1:DNA datasets collected under identical conditions in the absence of F01 showed negative Fo−Fc density when 8-oxoG was modeled, indicating that the excised base is not retained without the agonist (Supplementary Fig. 13).

We next examined F51[71], a slightly more potent *Hs*OGG1 agonist (Supplementary Fig. 14a–c). In contrast to F01, F51 density is clearly visible in the active site, at the position occupied by 8-oxoG in the *Hs*OGG1:DNA + F01 complex, indicating that F51 binds directly in the catalytic pocket rather than allosterically (Supplementary Fig. 14d-f). The density is consistent with a mixture of states: part of F51 is modeled too close to the 3′-PUA, implying that 3′-PUA either moves away or is absent when F51 is bound in the active site, and additional density, though weak, can be fit with a δ-elimination product whose occupancy is similar to that of F51. F51 binding also displaces K249 from the active site, weakening product binding (Supplementary Fig. 14e). This finding supports and extends the mechanism of action reported for the *Hs*OGG1 agonist TH10785 (compound C in reference[68]), which enhances activity by binding in the active site and promoting δ-elimination and product release (Supplementary Fig. 14f)[69]. Overall, our product-bound structures support a model in which agonists stimulate *Hs*OGG1 catalysis by enhancing the AP-lyase step and accelerating substrate turnover, either by stabilizing excised 8-oxoG in the active site or by occupying the active site to promote product release.

Discussion

Oxidized purines and pyrimidines are major forms of DNA damage across all domains of life, with repair initiation and biological outcomes dictated by damage-specific mono- and bifunctional DNA glycosylases. Bifunctional glycosylases fall primarily into two structural superfamilies: the helix–hairpin–helix (HhH) and the Fpg/Nei superfamilies. Yet a unified catalytic mechanism to guide biological understanding and therapeutic targeting has remained elusive for the HhH superfamily. Here, we establish a convergent, structure-based catalytic mechanism for two prototypic HhH bifunctional glycosylases: OGG1 and NTH1. Despite excising structurally divergent substrates, both enzymes rely on a conserved Asp−Lys dyad to execute their catalytic function. This contrasts with monofunctional HhH glycosylases, which lack the active-site lysine and proceed via a distinct oxocarbenium intermediate[8,12,53]. Ultimately, the mechanistic unity between OGG1 and NTH1 resolves a longstanding biochemical enigma, suggesting a conserved catalytic paradigm for bifunctional HhH glycosylases harboring this conserved Asp−Lys dyad.

Purine/pyrimidine glycosylase/lyases must first discriminate between damaged and undamaged bases. *Af*Ogg1 belongs to the OGG2 superfamily, whereas *Hs*OGG1 belongs to the OGG1 superfamily, with key catalytic residues and functional structural motifs conserved[72]. A major difference between OGG1 and OGG2 is how they distinguish 8-oxoG from G in the active site: *Hs*OGG1 uses a damage-specific interaction between 8-oxoG N7 and the backbone carbonyl of Gly42, whereas *Af*Ogg1 uses the extreme C-terminal carboxylate. Structurally, OGG2 family members lack the N-terminal A-domain present in OGG1. In *Hs*OGG1, this A-domain harbors Gly42 and shields its interaction with 8-oxoG. Sequence alignment of reviewed OGG2 entries in UniProt shows that *Af*Ogg1 is one of only two OGG2 enzymes with an additional N-terminal anti-parallel β-sheet that shields damage-specific interaction between 8-oxoG and the C-terminus, analogous to the A-domain in *Hs*OGG1. AF2-predicted structures suggest that in *Af*Ogg1 (and in *Aquifex aeolicus* Ogg) this N-terminal element appears necessary to stabilize C-terminal lesion recognition, whereas in the other OGG2 members the C-terminus is rigidified by a stable C-terminal hairpin, facilitated by the residue at the fourth position from the C-terminus.

For Tg processing enzymes, prior Tg-DNA structures showed no direct contacts between the enzymes and the oxidized thymine[24,47,73], suggesting Tg might be recognized before binding in the active site or via an indirect mechanism[47,55]. Our *Af*Nth1 pre-intermediate structure reveals the direct interactions between D46 and Tg hydroxyl groups at the C5-C6 positions, providing a mechanistic basis for lesion discrimination. Mutation of the equivalent D136 in *Hs*NTH1 severely impaired Tg excision, confirming its role in lesion detection. In the *Af*Nth1^{K122A} intermediate, Tg is bound without direct protein contacts, with only a water-mediated interaction between Tg C6-OH and a conserved S41, consistent with earlier Tg-bound inactive mutant structures[24,47,73]. By strengthening and providing missing structural data on both OGG and NTH glycosylases, we establish a foundation for a comprehensive, comparative mechanistic analysis of these bifunctional glycosylases. Notably, the conservation of a specific Asp-Lys dyad mechanism across Archaea and Humans suggests that it represents an ancient and optimized solution for coupling base excision to strand incision within a single active site, preserved through evolutionary selection.

Our integrated structural and computational interrogation of purine and pyrimidine glycosylase/lyases reveals both conserved and divergent features. *Hs*OGG1 selectively excises 8-oxoG most efficiently opposite C, whereas *Af*Ogg1 excises 8-oxoG even when paired with other bases, enabled by double flip of both 8-oxoG and its opposite nucleotide. To the best of our knowledge, this provides the structural evidence of double flipping of 8-oxoG and its opposite nucleotide for an 8-oxoG DNA glycosylase. In contrast, recent AGOG structures show that double flipping can happen from the damaged strand[74], proposed to explain relaxed opposite-base selectivity. However, prior studies on *Hs*OGG1 and OGG2 enzymes indicate that the opposite-base selectivity is primarily determined by the number and nature of contacts with the estranged base[31,75]. *Hs*OGG1 is highly selective for 8-oxoG opposite C due to multiple contacts made by R154 with C. This specificity is relaxed by the R154H mutation, which allows efficient cleavage of opposite A as well as C[31]. Double flipping of the damaged and estranged base has also been observed for other DNA glycosylases, including endonuclease IV[76], uracil DNA-glycosylase[77], MutY[78,79], and ALKBH2[80].

Our findings advance the mechanistic understanding of both OGG1 and NTH glycosylase/lyases[31,35], specifically informing on the differences in base binding, revealing distinct biochemical roles of excised bases for OGG1[31,35], and providing insights into the previously poorly characterized AP-lyase activity[38–41]. By integrating crystal structures and QM/MM simulations, we mapped the full reaction trajectories for both enzyme classes. We find that glycosidic C-N bond cleavage in Ogg1 and Nth1 does not proceed via an oxacarbenium ion intermediate, which is highly energetically disfavored ($\Delta G^{\ddagger} \approx 35$ kcal/mol). Instead, both enzymes use a ribose ring-opening mechanism in which a conserved Asp–Lys pair mediates protonation of the ribose, lowering the energy barrier to $\Delta G^{\ddagger} \approx 18$ kcal/mol. Thus, by exerting tight control over the protonation states of the attacking Lys and the ribose oxygen, the enzymes facilitate an iminium crosslink formation, which in turn lowers the barrier for glycosidic bond scission. This mechanistic dyad is supported by several structural observations: (1) *Af*Ogg1^{D140N} intermediate structure shows Asp controls the positioning of Lys; (2) Asp and Lys are in close proximity allowing proton sharing; and (3) proximity of Asp to the ribose oxygen atom enables hydrogen bonding with the nucleotide. These observations imply that for catalysis to occur, the catalytic Lys must remain neutral to initiate nucleophilic attack, meaning the proton is transferred to (or resides on) the Asp. This "ribose-protonated" mechanism is further supported by a recent *Hs*OGG1 crystal structure that directly captures a ring–opened ribose intermediate in a pH-sensitive K249H mutant under conditions favoring Asp protonation and concerted nucleophilic attack by a histidine-bound water[81]. However, because this mutant proceeds via hydrolysis rather than the nucleophilic attack by Lys, direct capture of the intermediate in WT OGG1 or NTH1 would be valuable to further corroborate this step in the native catalytic trajectory. Nonetheless, this structure provides strong suggestive evidence that ribose ring opening represents a viable mechanistic scenario. We also identified additional catalytic residues (E123 in *Af*Ogg1 and D46 in *Af*Nth1) that play important roles in catalysis. In *Af*Ogg1, E123 serves as the final proton acceptor, although 8-oxoG itself acts as a cofactor, facilitating proton shuttling and lowering the transition state energy. This effect is not seen in *Af*Nth1. Our simulations are in close alignment with biochemical findings supporting product-assisted catalysis for purine, but not pyrimidine glycosylases, such as *Ec*Nth1[31,35].

Despite the clear structural and biochemical evidence from our work and numerous prior reports demonstrating AP-lyase activity of *Hs*OGG1 in vitro, its biological relevance has been a matter of debate. OGG1 is often viewed as primarily monofunctional[50], with APE1 processing the resulting abasic site. This view is supported by the slower AP-lyase than glycosylase activity of OGG1[82], consistent with our computed barriers, and by the ability of APE1 to stimulate OGG1 turnover by product release[83,84]. APE1 cleavage at an abasic site generates a 5′-deoxyribose phosphate (5′-dRP) that is normally processed by Polβ 5′-dRP-lyase activity, which is essential for the short-patch BER[85]. In the absence of Polβ, however, repair can proceed through long-patch BER mediated by other DNA polymerases that use the 3′-OH group created by APE1 after removing 3′-PUA, an AP-lyase product of OGG1. Thus, the lyase product (3′-PUA) can channel repair toward high-fidelity polymerases, particularly at the replication fork. Nevertheless, the weak AP-lyase activity of OGG1 in vivo presents a therapeutic opportunity to enhance this step using small molecules that mimic or augment base-assisted catalysis. Our product-bound *Hs*OGG1 structure with an allosteric agonist F01 shows additional active-site electron density for bound 8-oxoG compared to the agonist-free product-bound state, supporting a cofactor-stabilizing mechanism, wherein allosteric agonists increase the residence time of the cleaved base, thereby promoting the AP-lyase reaction and increasing the overall turnover. In contrast, our *Hs*OGG1 structure with F51, a slightly more potent OGG1 agonist, shows clear density for F51 directly in the active site at the position previously occupied by 8-oxoG, indicating catalytic-site rather than allosteric binding. The structural and biochemical data indicate that F51 promotes δ-elimination in the active site, and F51 binding also displaces K249, weakening product binding. Thus, our agonist structures support a model in which *Hs*OGG1 agonists stimulate catalysis by enhancing the AP-lyase step and accelerating turnover, either by stabilizing excised 8-oxoG in the active site or by directly occupying the active site to promote product release.

An integrated OGG-NTH glycosylase/lyase catalytic mechanism has broad biological implications, as oxidized DNA damage and immune responses are interconnected[86], and OGG1 is linked to inflammation, oxygen metabolism and obesity[87]. Oxidative damage also has epigenetic roles, influencing transcription via BER[88]. Just as conservation of APE1 active site arginine (R177) from *E. coli* to humans over three billion years underscored its central role in BER[66], the analogous evolutionary conservation of catalytic lysine in both glycosylase and lyase steps of OGG and NTH argues for the biological significance of the lyase activity and supports the integrated mechanism reported here. This has potentially broad therapeutic relevance, as ionizing radiation and proton therapy generate oxidative DNA damage that recruits OGG1 and NTH1 capable of excising 8-oxoG and Tg, respectively, as part of a resistance pathway[89]. Multiple cancer-associated mutations in OGG1 and NTH1 affecting catalytic residues (Supplementary Data 1, 2) and oxidative stress is tightly linked to cancer and aging[90,91], suggesting catalysis-inspired chemical modulators of OGG1 and NTH1 may inform biology and medicine.

Our agonist-bound *Hs*OGG1 product structures provide sufficient active-site resolution in the presence of cleaved DNA, together with mechanistic insights from archaeal enzymes, to guide development of agonists and antagonists using compact Goldilocks libraries for virtual screens or experimental fragment libraries[92–94]. Importantly, we define crystal structures of intermediate states for 8-oxoG and Tg-bound glycosylase/lyases, enabling elucidation of the entire bifunctional reaction from a single active site for both purine- and pyrimidine-recognizing enzymes. The *Af*Nth1 pre-intermediate structure shows how Nth1 discriminates oxidized lesions from undamaged thymine before forming the intermediate state, and our simulations reveal similar key catalytic steps in OGG1 and NTH1, supporting co-evolution of bifunctional glycosylase/lyases for efficient catalysis in nucleosomes and damage surveillance of oxidation-prone chromatin sites[51,52]. Together, our product-bound structures of OGG1 with and without agonist highlight distinct roles of the excised base and small-molecule-mediated stimulation of OGG1 AP-lyase activity. Collectively, these findings define conserved and variable features of BER catalysis for oxidized base removal, with broad potential implications for cell biology and emerging precision therapies in cancer, aging, inflammation, neurodegeneration, and other diseases linked to genome stability and oxidative metabolism.

Methods

Protein purification, crystallization, and data collection

The WT and mutant *Af*Ogg1 were cloned and expressed from the pMAL-c2X plasmid and purified using the MBP-tag[60]. The affinity tag from the purified protein was cleaved, and the protein was dialyzed against a low-salt buffer (20 mM Tris (pH 7.4), 20 mM NaCl, 1 mM EDTA, 1 mM DTT). Protein was then further purified using MonoS cation exchange chromatography using a linear gradient of 20 mM- 1 M NaCl, and protein-containing fractions were collected. For crystallization experiments, purified WT, mutants, and selenomethionine (Se-Met)-substituted *Af*Ogg1 were concentrated to ~20 mg/mL in 10 mM HEPES (pH 7.5), 100 mM NaCl. Crystals of DNA-free WT Se-Met-substituted *Af*Ogg1 enzyme were grown by vapor diffusion from reservoir solutions containing 75% ammonium sulfate (saturated), 100 mM imidazole/malate pH 5.0. For cryoprotection, 20% ethylene glycol was added to the mother liquor. X-ray diffraction data were

collected from a single crystal at beamline 9-2 of the Stanford Synchrotron Radiation Laboratory (SSRL).

For the *Af*Ogg1-DNA complexes, *Af*Ogg1^{WT} (Se-Met) and *Af*Ogg1^{K122S}-mutant (native) enzymes were mixed in a 1:1 ratio with the blunt-ended, duplex 8-oxoG-containing DNA (5′-TAGAGTC(8-oxoG) ACCTGCA-3′ (Midland Certified Reagent Corp, Midland, TX)), in which the complementary strand had a cytosine opposite 8-oxoG and incubated on ice for 30 min. Similarly, AfOgg1^{D140N}-mutant (native) was mixed with 2 mM blunt-ended duplex 8-oxoG-containing DNA (5′-GCGTCCA(8-oxoG)GTCTACC-3′ (Midland Certified Reagent Corp, Midland, TX)) in which the complementary strand has a cytosine opposite 8-oxoG. Co-crystals were grown by hanging drop vapor diffusion from reservoir solutions containing 20–30% PEG4000, 100 mM MES buffer, pH 6.5, and 5% potassium permanganate (saturated). For cryoprotection, 20% ethylene glycol was added to the mother liquor. X-ray diffraction data were collected at beamline 11-1 of SSRL.

*Af*Nth1^{K122A} mutant coding sequence was cloned and expressed from the pET24a (Novogen) vector and purified from induced *E. coli* BL21 (DE3) cells[95]. For the Tg-containing substrate, a 13-mer 5′-ACGCGA(Tg)ACGCCA-3′ sequence was synthesized using the phosphoramidite building block for the oxidized base. Tg-containing strands were annealed to a complementary sequence 5′-TTGGCGTATCGCG-3′, leaving a single nt overhang on both ends and adenine as the opposite base to the Tg. For the *Af*Nth1^{WT}, the enzyme coding sequence was cloned and expressed from the pET (His-GST-TEV, Addgene#29655) vector. For the *Af*Nth1-DNA complexes, *Af*Nth1^{WT} or *Af*Nth1^{K122A} mutant enzymes were mixed in 1:1 ratio with the Tg-containing duplex and incubated on ice for 30 min. Since we obtained a pre-intermediate state in the case of the WT enzyme, we also purified the WT enzyme from an anaerobic Coy chamber (oxygen level <0.1 ppm), which made no difference with regard to crystal formation occurring only at low temperature (4 °C). We concluded that the product-bound state of AfNth1 was too flexible to crystallize. Crystals of pre-intermediate and intermediate states of *Af*Nth1-DNA complexes were obtained by hanging drop vapor diffusion from reservoir solutions containing 20–30% PEG8000, 100 mM imidazole/malonate (pH 4.5–5.5), 5 mM DTT, and 10% glycerol. Data for *Af*Nth1^{WT} and *Af*Nth1^{K122A} complexes were collected at beamlines 12-2 at SSRL and 5.0.1 at the Advanced Light Source (ALS), respectively.

*Hs*OGG1 (4-319 aa) coding sequence was cloned into a pET (His-GST-TEV, Addgene#29655)-based plasmid. His-GST was cleaved from the purified protein overnight in the cold room. Protein was then further purified using gel-filtration chromatography on Superdex200 Increase 10/300 GL (Cytiva). Protein-containing fractions were concentrated to 10 mg/mL in the gel-filtration buffer (40 mM Tris (pH 8.0), 200 mM NaCl, 1 mM TCEP). *Hs*OGG1 crystals in a DNA-free state were obtained by hanging drop vapor diffusion from a reservoir solution containing 100 mM sodium citrate (pH 5.0), 22% PEG6000, 5% ammonium sulfate (saturated). 25% ethylene glycol was used as a cryoprotectant for DNA-free *Hs*OGG1 crystals. The diffraction data were collected at the 12-2 beamline at SSRL. For the *Hs*OGG1-DNA complex, *Hs*OGG1 enzyme was mixed with an 8-oxoG-containing blunt-ended duplex in a 1:1 ratio and incubated on ice for 30 min. *Hs*OGG1:DNA crystals were obtained by hanging drop vapor diffusion from reservoir solutions containing 50 mM MES (pH 6.0), 16–23% PEG6000, with 25% ethylene glycol was used as cryoprotectant for *Hs*OGG1-DNA crystals. The diffraction data were collected at the beamline 8.3.1 at the ALS. For the *Hs*OGG1:DNA complex crystals in the presence of agonists F01/F51 (F01 was synthesized and characterized by the OHSU Medicinal Chemistry Core[71], and F51 was purchased from US Biologicals (cat# 164979), the same DNA substrate was used except that 4.5 mM of F01 or F51 were added to the crystallization conditions. Crystals were cryoprotected as described before, and the diffraction data were collected at the 12-2 beamline at SSRL.

Structure determination, refinement, and analysis

The *Af*Ogg1 structure was solved by SAD as follows: diffraction data on SeMet-incorporated enzyme were collected at the selenium anomalous peak (0.9791 Å) at SSRL. Diffraction data were processed using XDS[96], while phasing and model building were performed with phenix.autosol[97] and phenix.autobuild[98], respectively. Structure refinement was performed in phenix.refine[99] with iterative manual fitting using Coot[100]. For the *Af*Ogg1^{D140N} and *Af*Ogg1^{K122S} mutant complexes with DNA, the structures were solved by molecular replacement using the refined *Af*Ogg1^{WT} DNA-free structure. Diffraction data were processed using XDS (for *Af*Ogg1^{D140N} mutant) or the autoPROC pipeline[96,101–104] (for *Af*Ogg1^{K122S} mutant), and molecular replacement was performed with Phaser[105] as implemented in the Phenix suite[106]. Structure refinement was done in phenix.refine, with iterative manual model building and fitting in Coot[100]. Ligand restraints for 8-oxoG and molybdate were generated using phenix.ready_set. The structure of *Af*Ogg1^{WT}-product bound state was solved using the intermediate (*Af*Ogg1^{K122S}:DNA complex) structure for the molecular replacement, with the lesion omitted in the model. The ligand restraints for the 3′-PUA product were generated using eLBOW utility in the Phenix suite[107]. The PUA product was built into the difference density map in the active site and iterative structure refinement using phenix.refine and manual fitting in Coot were performed as described above. Data collection and refinement statistics are summarized in Supplementary Table 1.

*Af*Nth1^{K122A} mutant structure was solved by molecular replacement AmoRe[108]. A theoretical *Af*Nth1 starting model was built based on *Ec*EndoIII, and the MR search model was prepared by overlaying the theoretical model on *Ec* and *Bs*EndoIII structures. Initially, refinement was performed with CNS[109] and manual fitting with XFIT[110]. The model was further improved iteratively using phenix.refine suite and manual fitting in Coot. *Af*Nth1^{WT}:DNA complex structure was solved by using *Af*Nth1^{K122A}:DNA complex as an MR search model using Phaser as implemented in the Phenix suite. The ligand restraints for the Tg lesion (CTG) were generated using the eLBOW utility in the Phenix suite. The Tg lesion from the search model was omitted and rebuilt into the difference density. Structure refinement was done in phenix.refine, with iterative manual model building and fitting in Coot. Data collection and refinement statistics are summarized in Supplementary Table 2.

DNA-free *Hs*OGG1 structure was solved by molecular replacement using the previously published *Hs*OGG1 structure (PDB:5AN4[111]) as a search model in Phaser as implemented in the Phenix suite[106]. Structure refinement was performed in phenix.refine, with iterative manual model building and fitting in Coot. The DNA-free *Hs*OGG1 model was used to solve the structures of *Hs*OGG1:DNA in the presence or absence of F01 agonist. DNA sequence and ligands in the active site were built according to the density. Ligand restraints for excised base (OXG), F51, β-elimination product (3′-PUA), and the δ-elimination product (DEP) were generated using the eLBOW utility in the Phenix suite. Structure refinement was performed in phenix.refine, with iterative manual model building and fitting in Coot. For both HsOGG1:DNA structures in the presence or absence of F01 agonist, we solved multiple structures to analyze the flexibility in the active site region, but only one representative dataset for each condition was deposited in the PDB. Data collection and refinement statistics are summarized in Supplementary Table 3.

Mutagenesis and protein purification for enzymatic activity assays

*Af*Ogg1 (UniProt#O29876), *Af*Nth1 (UniProt#O28581), *Hs*OGG1 (UniProt#O15527, residues 12–327) and *Hs*NTH1 (UniProt#P78549, residues 83–312) coding sequences were cloned in pET (His-GST-TEV, Addgene#29655)-based expression plasmid. Mutations were introduced in these plasmids using site-directed mutagenesis by polymerase chain reaction.

*Hs*OGG1 WT and mutants were expressed in Rosetta™ cells and purified by TALON affinity chromatography. His-GST was cleaved from the purified proteins overnight at 4 °C, and the tag and TEV protease were removed by repassing the mixture over TALON resin. Proteins were further purified by gel-filtration chromatography on a Superdex200 increase 10/300. Protein-containing fractions were concentrated to 15.5 mg/mL (WT), 17.3 mg/mL (V250D), and 12.4 mg/mL (V250E) in gel-filtration buffer (40 mM Tris (pH 8.0), 200 mM NaCl, 1 mM TCEP), as determined by NanoDrop.

*Hs*NTH1 WT and mutants were similarly expressed in Rosetta™ cells. After affinity purification, the His-GST was cleaved overnight at 4 °C, and the tag and TEV protease were removed by repassing the mixture over TALON resin. Flow-through and low imidazole (10 mM) wash fractions containing *Hs*NTH1 were pooled and concentrated to 8.8 mg/mL (WT), 11.8 mg/mL (D136A), and 12.2 mg/mL (N271A) in dialysis buffer (25 mM Tris (pH 8.0), 300 mM NaCl, 5 mM β-ME), as determined by NanoDrop.

*Af*Ogg1 WT and E123A mutant were expressed and purified as described for *Hs*OGG1. After gel-filtration chromatography on Superdex200 increase 10/300, protein fractions were concentrated in 40 mM Tris (pH 8.0), 200 mM NaCl, 1 mM TCEP to 3 mg/mL (WT) and 0.57 mg/mL (E123A) as determined by NanoDrop.

*Af*Nth1 WT was expressed in Rosetta™ cells and purified by affinity chromatography followed by overnight His-GST cleavage at 4 °C and gel-filtration chromatography on Superdex200 Increase 10/300 GL. Protein-containing fractions were pooled and concentrated to 12.5 mg/mL in gel-filtration buffer (40 mM Tris (pH 8.0), 200 mM NaCl, 5 mM β-ME) as measured by BCA assay.

Fluorescence-based DNA glycosylase activity assays

DNA glycosylase activities were assayed using double-stranded oligodeoxynucleotides conjugated with a TAMRA fluorophore at the 5′ terminus of the lesion-containing strand and Black Hole Quencher 2 (BHQ2) at the 3′ terminus of the complementary strand. The TAMRA-labeled lesion-containing oligodeoxynucleotides were 17-mers and included the following sequences: (1) 5′-TAMRA-TCACC(8-oxoG)TCGTACGACTC-3′; (2) 5′-TAMRA-TCACCT(Tg)CGTACGACTC-3′; and (3) uracil-containing oligodeoxynucleotide 5′-TAMRA-TCACCUTCGTACGACTC-3′ used for generation of AP site-containing substrates. The complementary 3′-BHQ2-conjugated 17-mers were designed to contain a cytosine opposite 8-oxoG or the AP site for assays of *Af*Ogg1 and *Hs*OGG1 or an adenine opposite Tg or the AP site for assays of *Af*Nth1 and *Hs*NTH1. The 8-oxoG was synthetically incorporated into a 17-mer oligo[112]. All other oligodeoxynucleotides were purchased from Integrated DNA Technologies. For preparation of double-stranded DNA substrates, lesion-containing oligodeoxynucleotides (1 μM) were combined with complementary oligodeoxynucleotides (1.2 μM) in glycosylase reaction buffer (20 mM Tris-HCl buffer (pH 7.4), 100 mM KCl, and 0.01% (v/v) Tween-20), heated at 90 °C for 2 min, and slowly cooled to 4 °C. AP sites were generated by incubating U-containing oligodeoxynucleotides (100 nM) with 0.5 U/μl uracil DNA glycosylase (New England Biolabs Inc.) for 30 min at 37 °C in glycosylase reaction buffer supplemented with 100 μg/ml bovine serum albumin (BSA).

*Hs*NTH1, *Af*Nth1, and *Hs*OGG1 glycosylase activities were measured using 50 nM DNA substrate in glycosylase reaction buffer containing 100 μg/ml BSA, in a reaction volume of 20 μl. DNA substrates were aliquoted into a 384-well black flat-bottom microplate, and reactions were initiated by addition of enzyme dilutions using a multichannel pipette. Enzyme concentrations of 10, 100 and 1000 nM were used, with the latter two concentrations corresponding to single-turnover conditions. Fluorescence was monitored for 1 hour in a TECAN INFINITE M NANO instrument using a 525 nm (9 nm bandwidth) excitation filter and a 598 nm (20 nm bandwidth) emission filter, with relative fluorescence signal recorded for 60 min every 2 min at 37 °C. The initial rates of reactions were determined by fitting the linear portion of the reaction progress curve to a linear function using either Excel or Prism.

Compared to the other enzymes, *Af*Ogg1 exhibited a pronounced lag phase in initiating the glycosylase reaction at 37 °C. We previously reported *Af*Ogg1 glycosylase activity at 50 °C using gel-based assays[60]. However, our current fluorescence-based assay is not compatible with reactions at 50 °C; therefore, we measured the glycosylase activity of *Af*Ogg1 WT and the E123A mutant at 42 °C instead.

Gel-based DNA glycosylase activity assays

Oligonucleotides containing 8-oxoG were 5′-end-labeled with [γ-^{32}P] ATP (Revvity, Cat# BLU502A250UC) using T4 polynucleotide kinase (ThermoFisher, Cat# EK0031). Unincorporated labeled nucleotides were removed by MicroSpin G-25 columns (Cytiva, Cat# 27532501). Labeled oligonucleotides were annealed with 1.5-fold excess unlabeled complementary oligonucleotide in 10 mM HEPES-KOH (pH 7.8), 1 mM EDTA (HE), and 300 mM NaCl by heating at 90 °C for 3 min followed by gradual cooling to room temperature. The oligonucleotide sequences used were 5′-TAGAGTC(8-oxoG)ACCTGCA-3′ and the complementary strand 5′-TGCAGGTCGACTCTA-3′. The reactions were carried out in a reaction mixture (10 μl) that contained 26 nM *Hs*OGG1 and 10 nM ^{32}P-labeled oligonucleotide substrate with 2.5, 5, or 10 μM F51 in 50 mM Tris-HCl (pH 8.0), 75 mM NaCl, and 1 mM DTT. Reactions were incubated at 37 °C for 30 min and terminated by the addition of an equal volume of gel loading buffer (95% deionized formamide, 20 mM EDTA, 0.02% bromophenol blue, 0.02% xylene cyanol) followed by heating at 90 °C for 3 min. Reaction products were resolved by electrophoresis on a 16% denaturing polyacrylamide gel containing 8 M urea in 89 mM Tris-HCl, 89 mM boric acid and 2 mM EDTA (pH 8.0). Experiments were performed in three independent replicates.

AlphaFold modeling

The AF3 server (https://golgi.sandbox.google.com/)[113] was used to predict the model of *Hs*NTH1:DNA. The protein sequence for *Hs*NTH1 (UniProt accession # P78549) and a 13-mer duplex DNA sequence (ACGCCAT*ACGCCA, where the T* is an abasic site and paired with an A in the complementary strand) were used as input with default run parameters. AlphaFold2 model of the DNA-free structure of *Af*Nth1 was generated using a locally installed ColabFold on a GPU machine[114,115]. For the prediction, the protein sequence for *Af*Nth1 (UniProt accession# O28581) was used as input for alphafold2_multimer_v3 with default run parameters. Resulting models were deposited to the ModelArchive database (www.modelarchive.org).

Classical molecular dynamics

The classical molecular dynamics (MD) simulations were performed with the PMEMD module from the Amber22 software package[116,117]. The AMBER ff14SB force field was employed for the protein, while the OL15 force field was employed for the DNA. The parameters for the non-standard nucleotides thymine glycol (Tg) and 8-oxoguanine (8-oxoG) were developed using Antechamber. The charges and electrostatic potentials (ESP) were computed at the HF/6-31G(d,p) level of theory, after geometry optimization at the B3LYP/6-31G(d,p) level of theory using Gaussian 16 software[118]. The enzyme-substrate complex was then placed in a cubic box of 100x100x100 Å^3 dimensions. The shortest distance from the edge of the box to the surface of the complex was not shorter than 10 Å. The TIP3P water model was used as the solvent, and Na^+ and Cl^- ions were added to neutralize the total charge of the system and to achieve a concentration of 0.154 M. More details about the topology of the system are available in Supplementary Table 4.

After the initial minimization, the system was heated up to 300 K over 100 ns at constant volume (NVT), while imposing positional restraints of 100 kcal/(mol Å^2) on the heavy atoms. Subsequently, restraints were slowly removed, and to bridge the crystal structure, model building, and ab initio QM/MM simulations, we introduced a

200-ns equilibration stage (Supplementary Fig. 15), performed with classical MD using the isothermal-isobaric ensemble (NPT). The temperature control (300 K) was performed by a Langevin thermostat with a collision frequency of 1 ps^{-1}, and the pressure control (1 atm) was accomplished by a Monte Carlo barostat. The SHAKE algorithm was used to constrain the bonds involving hydrogen atoms, and the particle mesh Ewald method was used to compute the electrostatic interactions, which for both Coulombic and Van der Waals interactions, a 10 Å cutoff distance was maintained. The trajectories were computed with a time step of 1 fs. Cluster analysis was utilized to obtain the most representative structure from three independent simulations.

Quantum mechanics/molecular mechanics (QM/MM) molecular dynamics

The QM/MM Born-Oppenheimer MD simulations were performed using the CP2K code[119], which combines the QM program QUICKSTEP and the MM driver FIST. The electrostatic coupling between the QM and MM regions was computed using a real-space multigrid technique. The QM region of the system was simulated in a cubic box with sides of 20 Å. For the *Af*Nth1:DNA complex, the side chains of the amino acids D46, K122, Y130, D139, and N177, as well as the nucleotide Tg, were incorporated in the QM layer. In the *Af*Ogg1:DNA complex, the side chains of residues K122, E123, H126, R129, D140, and D185, together with the main chain (C-terminus) of K198 and the nucleotide 8-oxoG, comprise the QM layer. After completion of the MD simulations, water molecules remaining within hydrogen-bonding distance of the nucleotide and the active-site residues defining the QM region were systematically identified and incorporated into the QM model. This procedure resulted in the inclusion of four water molecules in *Af*Nth1 and two water molecules in *Af*Ogg1.

The QM region was treated at the BLYP-D3 level using a dual basis set of Gaussian and plane-waves (GPW). We employed a double zeta (MOLOPT) basis set along with an auxiliary PW basis set with a density cutoff of 320 Ry and Goedecker-Teter-Hutter (GTH) pseudopotentials. The remaining protein, DNA, ions, and solvent atoms were modeled in the MM part of the system, which was described using the same AMBER ff14SB /OL15 force fields parameters employed as in the classical MD simulations. The simulations were performed in a NVT ensemble (300 K), employing a velocity rescaling thermostat. A time step of 0.5 fs was employed during the 50 ps of simulations. Cluster analysis was utilized to obtain the most representative structure from three independent simulations. MD simulation reliability and reproducibility checklist is provided as Supplementary Table 5.

QM/MM metadynamics

The free energy surfaces for each chemical reaction were obtained using metadynamics (MTD) simulations as implemented in the CP2K code. Each MTD simulation was performed utilizing a single collective variable (CV). CV1 is the difference in the distance between the NK atom of the lysine residue and the C1′ atom of the ribose and the distance (length) of the O4′-C1′ bond in the ribose. CV2 is the addition of the distances (lengths) of the NK-HK bond in the lysine residue and the C1′-N1 bond in the nucleotide. CV3 is the difference in the distance between the OW atom of the water molecule and the C1′ atom of the ribose and the distance (length) of the OW-HW bond in the water molecule. CV4 is the difference in the distance between the NK atom of the lysine residue and the C1′ atom of the ribose and the distance of the HW atom (from the OH group bound to the ribose) and the OD atom of the aspartic acid residue. CV5 is the difference in the distance between the H2 atom of the ribose and the OW atom of the water molecule and the distance (length) of the C3′-O3 bond in the phosphate group. Gaussian hills with a height of 0.5 – 1 kcal/mol and a width of 0.1–0.2 Å were placed in the CV space every 100 fs. Quadratic walls were used to restrict the exploration of the free energy surface around the reactive region. The simulation was considered complete after the re-crossing event from the reactants to the products and back occurred.

Reporting summary

Further information on research design is available in the Nature Portfolio Reporting Summary linked to this article.

Data availability

All crystallographic data and respective structural models generated in this study have been deposited to the Protein Data Bank (PDB) with accession numbers: 9O00 (DNA-free AfOgg1 structure), 9O01 (8-oxoG-DNA:AfOgg1^{D140N} structure), 9O02 (8-oxoG-DNA:AfOgg1^{K122S} structure), 9O03 (8-oxoG-DNA:AfOgg1^{WT} structure), 9NZC (Tg-DNA:AfNth1^{WT} structure), 9NZD (Tg-DNA:AfNth1^{K122A} structure), 9NZ8 (DNA-free HsOGG1 structure), 9NZ9 (8-oxoG-DNA:HsOGG1^{WT} structure), 9NZA (8oxoG-DNA:HsOGG1^{WT} in the presence of F01 agonist structure) and 10MN (8oxoG-DNA:HsOGG1^{WT} in the presence of F51 agonist). Computational models generated in this study have been deposited to ModelArchive repository with accession numbers: ma-smaw3 (*Af*Ogg1-reactant ($\mathbf{R}_{AfOgg1}$) model), ma-tklfr (*Af*Ogg1-intermediate 1 ($\mathbf{I1}_{AfOgg1}$) model), ma-m3xhj (*Af*Ogg1-intermediate 3 ($\mathbf{I3}_{AfOgg1}$) model), ma-3mblu (*Af*Ogg1-intermediate 4 ($\mathbf{I4}_{AfOgg1}$) model), ma-zz93j (*Af*Ogg1-intermediate 5 ($\mathbf{I5}_{AfOgg1}$) model), ma-eimct (*Af*Ogg1-product ($\mathbf{P}_{AfOgg1}$) model), ma-e19o7 (*Af*Nth1-reactant ($\mathbf{R}_{AfNth1}$) model), ma-va1dd (*Af*Nth1-intermediate 1 ($\mathbf{I1}_{AfNth1}$) model), ma-4ajp6 (*Af*Nth1-intermediate 3 ($\mathbf{I3}_{AfNth1}$) model), ma-035aq (*Af*Nth1-intermediate 4 ($\mathbf{I4}_{AfNth1}$) model), ma-18kfi (*Af*Nth1-intermediate 5 ($\mathbf{I5}_{AfNth1}$) model), and ma-c5vm6 (*Af*Nth1-product ($\mathbf{P}_{AfNth1}$) model). Also, ma-p43d2 (AF2-predicted structure of AfNth1 in DNA-free state model) and ma-765nw (AF3-predicted structure of HsNTH1 bound to dsDNA duplex with an abasic site model). All other data generated in this study are included in this article or in the supplementary information. Further requests for reagents and resources should be directed to and will be fulfilled by the corresponding authors. Source data are provided with this paper.

References

1. Lindahl, T. Instability and decay of the primary structure of DNA. *Nature* **362**, 709–715 (1993).
2. Barnes, D. E. & Lindahl, T. Repair and Genetic Consequences of Endogenous DNA Base Damage in Mammalian Cells. *Annu. Rev. Genet.* **38**, 445–476 (2004).
3. Lindahl, T. & Barnes, D. E. Repair of Endogenous DNA Damage. *Cold Spring Harb. Symposia Quant. Biol.* **65**, 127–134 (2000).
4. Tubbs, A. & Nussenzweig, A. Endogenous DNA Damage as a Source of Genomic Instability in Cancer. *Cell* **168**, 644–656 (2017).
5. Chatterjee, N. & Walker, G. C. Mechanisms of DNA damage, repair, and mutagenesis. *Environ. Mol. Mutagenes.* **58**, 235–263 (2017).
6. Wallace, S. S. Base excision repair: A critical player in many games. *DNA Repair* **19**, 14–26 (2014).
7. Huffman, J. L., Sundheim, O. & Tainer, J. A. DNA base damage recognition and removal: New twists and grooves. *Mutat. Res. /Fundam. Mol. Mech. Mutagenes.* **577**, 55–76 (2005).
8. Trasviña-Arenas, C. H., Demir, M., Lin, W.-J. & David, S. S. Structure, function and evolution of the Helix-hairpin-Helix DNA glycosylase superfamily: Piecing together the evolutionary puzzle of DNA base damage repair mechanisms. *DNA Repair*. **108**, https://doi.org/10.1016/j.dnarep.2021.103231 (2021).
9. Hitomi, K., Iwai, S. & Tainer, J. A. The intricate structural chemistry of base excision repair machinery: Implications for DNA damage recognition, removal, and repair. *DNA Repair* **6**, 410–428 (2007).
10. Slupphaug, G. et al. A nucleotide-flipping mechanism from the structure of human uracil–DNA glycosylase bound to DNA. *Nature* **384**, 87–92 (1996).
11. Tubbs, J. L. et al. Flipping of alkylated DNA damage bridges base and nucleotide excision repair. *Nature* **459**, 808–813 (2009).

12. Mullins, E. A., Rodriguez, A. A., Bradley, N. P. & Eichman, B. F. Emerging Roles of DNA Glycosylases and the Base Excision Repair Pathway. *Trends Biochem. Sci.* **44**, 765–781 (2019).
13. Izumi, T. et al. Mammalian DNA base excision repair proteins: their interactions and role in repair of oxidative DNA damage. *Toxicology* **193**, 43–65 (2003).
14. Krokan, H. E. & Bjoras, M. Base Excision Repair. *Cold Spring Harb. Perspect. Biol.* **5**, a012583–a012583 (2013).
15. Caliri, A. W., Tommasi, S. & Besaratinia, A. Relationships among smoking, oxidative stress, inflammation, macromolecular damage, and cancer. *Mutation Res./Rev. Mutation Res.* **787**, https://doi.org/10.1016/j.mrrev.2021.108365 (2021).
16. Cadet, J. & Wagner, J. R. DNA base damage by reactive oxygen species, oxidizing agents, and UV radiation. *Cold Spring Harb. Perspect. Biol.* **5**, a012559–a012559 (2013).
17. Flora, S. J. S. Arsenic-induced oxidative stress and its reversibility. *Free Radic. Biol. Med.* **51**, 257–281 (2011).
18. Cooke, M. S., Evans, M. D., Dizdaroglu, M. & Lunec, J. Oxidative DNA damage: mechanisms, mutation, and disease. *FASEB J.* **17**, 1195–1214 (2003).
19. Dizdaroglu, M., Coskun, E. & Jaruga, P. Measurement of oxidatively induced DNA damage and its repair by mass spectrometric techniques. *Free Radic. Res.* **49**, 525–548 (2015).
20. Ide, H., Kow, Y. W. & Wallace, S. S. Thymine glycols and urea residues in M13 DNA constitute replicative blocks in vitro. *Nucleic Acids Res.* **13**, 8035–8052 (1985).
21. Clark, J. M. & Beardsley, G. P. Thymlne glycol lesions terminate chain elongation by DNA polymerase I in vitro. *Nucleic Acids Res.* **14**, 737–749 (1986).
22. McNulty, J. M., Jerkovic, B., Bolton, P. H. & Basu, A. K. Replication inhibition and miscoding properties of DNA templates containing a site-specific cis-Thymine glycol or urea residue. *Chem. Res. Toxicol.* **11**, 666–673 (1998).
23. Evans, J. et al. Thymine ring saturation and fragmentation products: lesion bypass, misinsertion and implications for mutagenesis. *Mutat. Res./Genet. Toxicol.* **299**, 147–156 (1993).
24. Aller, P., Rould, M. A., Hogg, M., Wallace, S. S. & Doublié, S. A structural rationale for stalling of a replicative DNA polymerase at the most common oxidative thymine lesion, thymine glycol. *Proc. Natl. Acad. Sci.* **104**, 814–818 (2007).
25. O'Neill, P. Pulse Radiolytic Study of the Interaction of Thiols and Ascorbate with OH Adducts of dGMP and dG: Implications for DNA Repair Processes. *Radiat. Res.* **96**, https://doi.org/10.2307/3576178 (1983).
26. Michaels, M. L. & Miller, J. H. The GO system protects organisms from the mutagenic effect of the spontaneous lesion 8-hydroxyguanine (7,8-dihydro-8-oxoguanine). *J. Bacteriol.* **174**, 6321–6325 (1992).
27. Shibutani, S., Takeshita, M. & Grollman, A. P. Insertion of specific bases during DNA synthesis past the oxidation-damaged base 8-oxodG. *Nature* **349**, 431–434 (1991).
28. Lu, R., Nash, H. M. & Verdine, G. L. A mammalian DNA repair enzyme that excises oxidatively damaged guanines maps to a locus frequently lost in lung cancer. *Curr. Biol.* **7**, 397–407 (1997).
29. Bjoras, M. Opposite base-dependent reactions of a human base excision repair enzyme on DNA containing 7,8-dihydro-8-oxoguanine and abasic sites. *EMBO J.* **16**, 6314–6322 (1997).
30. Aburatani, H. et al. Cloning and characterization of mammalian 8-hydroxyguanine-specific DNA glycosylase/apurinic, apyrimidinic lyase, a functional mutM homologue. *Cancer Res.* **57**, 2151–2156 (1997).
31. Bruner, S. D., Norman, D. P. G. & Verdine, G. L. Structural basis for recognition and repair of the endogenous mutagen 8-oxoguanine in DNA. *Nature* **403**, 859–866 (2000).
32. Demple, B. & Linn, S. DNA N-glycosylases and UV repair. *Nature* **287**, 203–208 (1980).
33. Kuo, C.-F. et al. Atomic Structure of the DNA Repair [4Fe-4S] Enzyme Endonuclease III. *Science* **258**, 434–440 (1992).
34. Thayer, M. M., Ahern, H., Xing, D., Cunningham, R. P. & Tainer, J. A. Novel DNA binding motifs in the DNA repair enzyme endonuclease III crystal structure. *EMBO J.* **14**, 4108–4120 (1995).
35. Fromme, J. C. Structure of a trapped endonuclease III-DNA covalent intermediate. *EMBO J.* **22**, 3461–3471 (2003).
36. Carroll, B. L. et al. Caught in motion: human NTHL1 undergoes interdomain rearrangement necessary for catalysis. *Nucleic Acids Res.* **49**, 13165–13178 (2021).
37. David, S. S., O'Shea, V. L. & Kundu, S. Base-excision repair of oxidative DNA damage. *Nature* **447**, 941–950 (2007).
38. Sadeghian, K. & Ochsenfeld, C. Unraveling the base excision repair mechanism of human DNA Glycosylase. *J. Am. Chem. Soc.* **137**, 9824–9831 (2015).
39. Šebera, J. et al. The mechanism of the glycosylase reaction with hOGG1 base-excision repair enzyme: concerted effect of Lys249 and Asp268 during excision of 8-oxoguanine. *Nucleic Acids Res.* **45**, 5231–5242 (2017).
40. Tyugashev, T. E. et al. Roles of active-site amino acid residues in specific recognition of DNA lesions by human 8-Oxoguanine-DNA Glycosylase (OGG1). *J. Phys. Chem. B* **123**, 4878–4887 (2019).
41. McKibbin, P. L., Kobori, A., Taniguchi, Y., Kool, E. T. & David, S. S. Surprising repair activities of nonpolar analogs of 8-oxoG expose features of recognition and catalysis by base excision repair glycosylases. *J. Am. Chem. Soc.* **134**, 1653–1661 (2012).
42. Ren, M. et al. Structural basis for human OGG1 processing 8-oxodGuo within nucleosome core particles. *Nat. Commun.* **15**, https://doi.org/10.1038/s41467-024-53811-3 (2024).
43. Cordero, C. et al. Contributing factors to the oxidation-induced mutational landscape in human cells. *Nat. Commun,* **15**, https://doi.org/10.1038/s41467-024-55497-z (2024).
44. Fromme, J. C., Bruner, S. D., Yang, W., Karplus, M. & Verdine, G. L. Product-assisted catalysis in base-excision DNA repair. *Nat. Struct. Mol. Biol.* **10**, 204–211 (2003).
45. Kuznetsov, N. A. Kinetics of substrate recognition and cleavage by human 8-oxoguanine-DNA glycosylase. *Nucleic Acids Res.* **33**, 3919–3931 (2005).
46. Eckenroth, B. E., Cao, V. B., Averill, A. M., Dragon, J. A. & Doublié, S. Unique structural features of mammalian NEIL2 DNA glycosylase prime its activity for diverse DNA substrates and environments. *Structure* **29**, 29–42.e24 (2021).
47. Imamura, K., Averill, A., Wallace, S. S. & Doublié, S. Structural Characterization of viral ortholog of human DNA Glycosylase NEIL1 bound to Thymine Glycol or 5-Hydroxyuracil-containing DNA. *J. Biol. Chem.* **287**, 4288–4298 (2012).
48. Rodriguez, A. A. et al. An autoinhibitory role for the GRF zinc finger domain of DNA glycosylase NEIL3. *J. Biol. Chem.* **295**, 15566–15575 (2020).
49. Liu, M., Imamura, K., Averill, A. prilM., Wallace, S. usanS. & Doublié, S. Structural characterization of a mouse ortholog of human NEIL3 with a marked preference for single-stranded DNA. *Structure* **21**, 247–256 (2013).
50. Dalhus, B. et al. Separation-of-function mutants unravel the dual-reaction mode of human 8-Oxoguanine DNA Glycosylase. *Structure* **19**, 117–127 (2011).
51. Maher, R. L., Wallace, S. S. & Pederson, D. S. The lyase activity of bifunctional DNA glycosylases and the 3′-diesterase activity of APE1 contribute to the repair of oxidized bases in nucleosomes. *Nucleic Acids Res.* **47**, 2922–2931 (2019).
52. Bacolla, A. et al. Heritable pattern of oxidized DNA base repair coincides with pre-targeting of repair complexes to open chromatin. *Nucleic Acids Res.* **49**, 221–243 (2021).

53. Werner, R. M. & Stivers, J. T. Kinetic isotope effect studies of the reaction catalyzed by Uracil DNA glycosylase: evidence for an Oxocarbenium Ion–Uracil anion intermediate. *Biochemistry* **39**, 14054–14064 (2000).
54. Sadeghian, K. et al. Ribose-protonated DNA base excision repair: a combined theoretical and experimental study. *Angew. Chem. Int. Ed.* **53**, 10044–10048 (2014).
55. Zhu, C. et al. Tautomerization-dependent recognition and excision of oxidation damage in base-excision DNA repair. *Proc. Natl. Acad. Sci.* **113**, 7792–7797 (2016).
56. McCullough, A. K., Dodson, M. L. & Lloyd, R. S. Initiation of base excision repair: glycosylase mechanisms and structures. *Annu. Rev. Biochem.* **68**, 255–285 (1999).
57. Guan, Y. et al. MutY catalytic core, mutant and bound adenine structures define specificity for DNA repair enzyme superfamily. *Nat. Struct. Biol.* **5**, 1058–1064 (1998).
58. van der Kemp, P. A. Catalytic and DNA-binding properties of the human Ogg1 DNA N-glycosylase/AP lyase: biochemical exploration of H270, Q315 and F319, three amino acids of the 8-oxoguanine-binding pocket. *Nucleic Acids Res.* **32**, 570–578 (2004).
59. Norman, D. P. G., Chung, S. J. & Verdine, G. L. Structural and biochemical exploration of a critical amino acid in human 8-Oxoguanine glycosylase. *Biochemistry* **42**, 1564–1572 (2003).
60. Hyung Chung, J., Suh, M.-J., In Park, Y., Tainer, J. A. & Sun Han, Y. Repair activities of 8-oxoguanine DNA glycosylase from Archaeoglobus fulgidus, a hyperthermophilic archaeon. *Mutat. Res./DNA Repair* **486**, 99–111 (2001).
61. Hollis, T., Ichikawa, Y. & Ellenberger, T. DNA bending and a flip-out mechanism for base excision by the helix–hairpin–helix DNA glycosylase, Escherichia coli AlkA. *EMBO J.* **19**, 758–766 (2000).
62. Crenshaw, C. M. et al. Enforced presentation of an extrahelical Guanine to the lesion recognition pocket of human 8-Oxoguanine Glycosylase, hOGG1. *J. Biol. Chem.* **287**, 24916–24928 (2012).
63. Calvaresi, M., Bottoni, A. & Garavelli, M. Computational clues for a new mechanism in the glycosylase activity of the human DNA Repair Protein hOGG1. A generalized paradigm for purine-repairing systems? *J. Phys. Chem. B* **111**, 6557–6570 (2007).
64. Gates, K. S. An overview of chemical processes that damage cellular DNA: spontaneous hydrolysis, alkylation, and reactions with radicals. *Chem. Res. Toxicol.* **22**, 1747–1760 (2009).
65. Kane, C. M. & Linn, S. Purification and characterization of an apurinic/apyrimidinic endonuclease from HeLa cells. *J. Biol. Chem.* **256**, 3405–3414 (1981).
66. Mol, C. D., Izumi, T., Mitra, S. & Tainer, J. A. DNA-bound structures and mutants reveal abasic DNA binding by APE1 DNA repair and coordination. *Nature* **403**, 451–456 (2000).
67. Lenz, S. A. P., Kellie, J. L. & Wetmore, S. D. Glycosidic bond cleavage in DNA nucleosides: effect of nucleobase damage and activation on the mechanism and barrier. *J. Phys. Chem. B* **119**, 15601–15612 (2015).
68. Baptiste, B. A. et al. Enhanced mitochondrial DNA repair of the common disease-associated variant, Ser326Cys, of hOGG1 through small molecule intervention. *Free Radic. Biol. Med.* **124**, 149–162 (2018).
69. Michel, M. et al. Small-molecule activation of OGG1 increases oxidative DNA damage repair by gaining a new function. *Science* **376**, 1471–1476 (2022).
70. Tian, G. et al. Small molecule-mediated allosteric activation of the base excision repair enzyme 8-oxoguanine DNA glycosylase and its impact on mitochondrial function. *Sci. Rep.* **12**, https://doi.org/10.1038/s41598-022-18878-2 (2022).
71. Luzadder, M. M. et al. Small molecule agonists of 8-oxoguanine DNA glycosylase, OGG1. *bioRXiv*. https://doi.org/10.64898/2026.01.30.702659 (2026).
72. Faucher, F., Doublié, S. & Jia, Z. 8-Oxoguanine DNA Glycosylases: One Lesion, Three Subfamilies. *Int. J. Mol. Sci.* **13**, 6711–6729 (2012).
73. Aller, P., Duclos, S., Wallace, S. S. & Doublié, S. A crystallographic study of the role of sequence context in thymine glycol bypass by a replicative DNA polymerase serendipitously sheds light on the Exonuclease complex. *J. Mol. Biol.* **412**, 22–34 (2011).
74. Franck, C. et al. Structural and functional determinants of the archaeal 8-oxoguanine-DNA glycosylase AGOG for DNA damage recognition and processing. *Nucleic Acids Res.* **50**, 11072–11092 (2022).
75. Faucher, F., Duclos, S., Bandaru, V., Wallace, S. S. & Doublié, S. Crystal structures of two Archaeal 8-Oxoguanine DNA Glycosylases provide structural insight into Guanine/8-Oxoguanine distinction. *Structure* **17**, 703–712 (2009).
76. Hosfield, D. J., Guan, Y., Haas, B. J., Cunningham, R. P. & Tainer, J. A. Structure of the DNA repair enzyme Endonuclease IV and Its DNA complex. *Cell* **98**, 397–408 (1999).
77. Parikh, S. S. et al. Uracil-DNA glycosylase–DNA substrate and product structures: Conformational strain promotes catalytic efficiency by coupled stereoelectronic effects. *Proc. Natl. Acad. Sci.* **97**, 5083–5088 (2000).
78. House, P. G. et al. in *Base Excision Repair Progress in Nucleic Acid Research and Molecular Biology* 349–364 (2001).
79. Bernards, A. S., Miller, J. K., Bao, K. K. & Wong, I. Flipping Duplex DNA Inside Out. *J. Biol. Chem.* **277**, 20960–20964 (2002).
80. Yi, C. et al. Duplex interrogation by a direct DNA repair protein in search of base damage. *Nat. Struct. Mol. Biol.* **19**, 671–676 (2012).
81. Unno, M. et al. Capturing a glycosylase reaction intermediate in DNA repair by freeze-trapping of a pH-responsive hOGG1 mutant. *Nucl. Acids Res.* **53**, https://doi.org/10.1093/nar/gkaf718 (2025).
82. Zharkov, D. O., Rosenquist, T. A., Gerchman, S. E. & Grollman, A. P. Substrate specificity and reaction mechanism of Murine 8-Oxoguanine-DNA Glycosylase. *J. Biol. Chem.* **275**, 28607–28617 (2000).
83. Hill, J. W. Stimulation of human 8-oxoguanine-DNA glycosylase by AP-endonuclease: potential coordination of the initial steps in base excision repair. *Nucleic Acids Res.* **29**, 430–438 (2001).
84. Vidal, A. E. Mechanism of stimulation of the DNA glycosylase activity of hOGG1 by the major human AP endonuclease: bypass of the AP lyase activity step. *Nucleic Acids Res.* **29**, 1285–1292 (2001).
85. Allinson, S. L. DNA polymerase beta is the major dRP lyase involved in repair of oxidative base lesions in DNA by mammalian cell extracts. *EMBO J.* **20**, 6919–6926 (2001).
86. Ye, Z., Shi, Y., Lees-Miller, S. P. & Tainer, J. A. Function and Molecular Mechanism of the DNA Damage Response in Immunity and Cancer Immunotherapy. *Front. Immunol.* **12**, https://doi.org/10.3389/fimmu.2021.797880 (2021).
87. Komakula, S. S. B. et al. The DNA repair protein OGG1 protects against obesity by altering mitochondrial energetics in white adipose tissue. *Sci. Rep.* **8**, https://doi.org/10.1038/s41598-018-33151-1 (2018).
88. Fleming, A. M., Ding, Y. & Burrows, C. J. Oxidative DNA damage is epigenetic by regulating gene transcription via base excision repair. *Proc. Natl. Acad. Sci.* **114**, 2604–2609 (2017).
89. Robeska, E. et al. Targeted nuclear irradiation with a proton microbeam induces oxidative DNA base damage and triggers the recruitment of DNA glycosylases OGG1 and NTH1. *DNA Repair* **133**, https://doi.org/10.1016/j.dnarep.2023.103610 (2024).
90. Maynard, S., Schurman, S. H., Harboe, C., de Souza-Pinto, N. C. & Bohr, V. A. Base excision repair of oxidative DNA damage and association with cancer and aging. *Carcinogenesis* **30**, 2–10 (2008).

91. Das, L., Quintana, V. G. & Sweasy, J. B. NTHL1 in genomic integrity, aging and cancer. *DNA Repair* **93,** https://doi.org/10.1016/j.dnarep.2020.102920 (2020).
92. Moiani, D. & Tainer, J. A. A goldilocks computational protocol for inhibitor discovery targeting DNA damage responses including replication-repair functions. *Front. Mol. Biosci.* **11,** https://doi.org/10.3389/fmolb.2024.1442267 (2024).
93. Shibata, A. et al. DNA Double-Strand Break Repair Pathway Choice Is Directed by Distinct MRE11 Nuclease Activities. *Mol. Cell* **53**, 7–18 (2014).
94. Newman, J. A. et al. Structure, mechanism and crystallographic fragment screening of the SARS-CoV-2 NSP13 helicase. *Nat. Commun.* **12**, https://doi.org/10.1038/s41467-021-25166-6 (2021).
95. Shekhtman, A., McNaughton, L., Cunningham, R. P. & Baxter, S. M. Identification of the Archaeoglobus fulgidus endonuclease III DNA interaction surface using heteronuclear NMR methods. *Structure* **7**, 919–930 (1999).
96. Kabsch, W. Xds. *Acta Crystallogr. D. Biol. Crystallogr.* **66**, 125–132 (2010).
97. Terwilliger, T. C. et al. Decision-making in structure solution using Bayesian estimates of map quality: thePHENIX AutoSolwizard. *Acta Crystallogr. D. Biol. Crystallogr.* **65**, 582–601 (2009).
98. Terwilliger, T. C. et al. Iterative model building, structure refinement and density modification with thePHENIX AutoBuildwizard. *Acta Crystallogr. D. Biol. Crystallogr.* **64**, 61–69 (2007).
99. Afonine, P. V. et al. Towards automated crystallographic structure refinement with phenix.refine. *Acta Crystallogr. D. Biol. Crystallogr.* **68**, 352–367 (2012).
100. Emsley, P., Lohkamp, B., Scott, W. G. & Cowtan, K. Features and development of Coot. *Acta Crystallogr. D. Biol. Crystallogr.* **66**, 486–501 (2010).
101. Vonrhein, C. et al. Data processing and analysis with the autoPROC toolbox. *Acta Crystallogr. D. Biol. Crystallogr.* **67**, 293–302 (2011).
102. Evans, P. Scaling and assessment of data quality. *Acta Crystallogr. D. Biol. Crystallogr.* **62**, 72–82 (2005).
103. Evans, P. R. & Murshudov, G. N. How good are my data and what is the resolution? *Acta Crystallogr. D. Biol. Crystallogr.* **69**, 1204–1214 (2013).
104. Agirre, J. et al. The CCP4 suite: integrative software for macromolecular crystallography. *Acta Crystallogr. D. Struct. Biol.* **79**, 449–461 (2023).
105. McCoy, A. J. et al. Phasercrystallographic software. *J. Appl. Crystallogr.* **40**, 658–674 (2007).
106. Liebschner, D. et al. Macromolecular structure determination using X-rays, neutrons and electrons: recent developments in Phenix. *Acta Crystallogr. D. Struct. Biol.* **75**, 861–877 (2019).
107. Moriarty, N. W., Grosse-Kunstleve, R. W. & Adams, P. D. Electronic Ligand Builder and Optimization Workbench(eLBOW): a tool for ligand coordinate and restraint generation. *Acta Crystallogr. D. Biol. Crystallogr.* **65**, 1074–1080 (2009).
108. Navaza, J. Implementation of molecular replacement in AMoRe. *Acta Crystallogr. D. Biol. Crystallogr.* **57**, 1367–1372 (2001).
109. Brünger, A. T. et al. Crystallography & NMR system: a new software suite for macromolecular structure determination. *Acta Crystallogr. D. Biol. Crystallogr.* **54**, 905–921 (1998).
110. McRee, D. E. XtalView/Xfit—A versatile program for manipulating atomic coordinates and electron density. *J. Struct. Biol.* **125**, 156–165 (1999).
111. Zander, U. et al. Automated harvesting and processing of protein crystals through laser photoablation. *Acta Crystallogr. D. Struct. Biol.* **72**, 454–466 (2016).
112. Volkert, M. R. et al. Inhibition of DNA glycosylases via small molecule purine analogs. *PLoS ONE* **8**, https://doi.org/10.1371/journal.pone.0081667 (2013).
113. Abramson, J. et al. Accurate structure prediction of biomolecular interactions with AlphaFold 3. *Nature* **630**, 493–500 (2024).
114. Jumper, J. et al. Highly accurate protein structure prediction with AlphaFold. *Nature* **596**, 583–589 (2021).
115. Mirdita, M. et al. ColabFold: making protein folding accessible to all. *Nat. Methods* **19**, 679–682 (2022).
116. Case, D. A. et al. AmberTools. *J. Chem. Inf. Model.* **63**, 6183–6191 (2023).
117. Amber 2024 University of California, San Francisco, CA, (2024).
118. Gaussian 16 v. Revision C.01. Gaussian, Inc., Wallingford, CT, (2016).
119. Kühne, T. D. et al. CP2K: An electronic structure and molecular dynamics software package - Quickstep: Efficient and accurate electronic structure calculations. *J. Chem. Phys.* **152**, https://doi.org/10.1063/5.0007045 (2020).

Acknowledgements

We thank Drs. Ji Hyung Chung and Ye Sun Han for providing an initial protein sample, C. Hitomi for assistance with protein purification, and SSRL and ALS staff for assistance with diffraction data collection and facilities. We also thank Drs. A. D. D'Andrea, C. Yan, S. Tsutakawa, C. Trame, J. L. Tubbs, S. Matsuda, J.-L. Bodmer, B. R. Chapados, D. S. Daniels, C. D. Putnam, J. Holton, E. D. Getzoff, and D. P. Barondeau for many helpful discussions.

Author contributions

A.Syed, R.S.L., I.I., and J.A.T.: conceived and directed the study. A.Syed, A.S.A., I.G.M., J.L.H., C.D.M., K.H., A.H.S., S.P., C-L.T., S.I., and D.S.S.: performed experiments. L.F.S. and I.I.: performed the computational analyses and interpretation. A.Syed, A.S.A., I.G.M., H.Y.H.T., J.L.H., C.D.M., K.H., A.H.S., S.P., C.-L.T., A.B., D.S.S. R.S.L., and J.A.T: data curation, analysis, and interpretation. R.P.C., S.I., D.C., R.S.L., I.I., and J.A.T.: provided oversight. A.Syed, L.F.S., I.I., and J.A.T.: wrote and revised the manuscript with input from all co-authors.

Funding statements

A.Syed acknowledges support from the Claudia Adams Barr Program in Innovative Basic Cancer Research at the Dana-Farber Cancer Institute and the Joint Center for Radiation Therapy Foundation grant. J.A.T. is a Robert A. Welch Chair in Chemistry at the University of Texas MD Anderson Cancer Center (G-0010). This work was also supported by the National Institutes of Health (R35 CA220430, GM46312, CA97209, and P01 CA092584 to J.A.T. and I.I., and HL07781 to J.L.H.), the National Institute of General Medical Sciences (R35 GM139382 to I.I.), the National Institute of Environmental Health Sciences (R01 ES032786 to I.I.), and the National Science Foundation (MCB-2027902 to I.I.), the Human Frontiers in Science Program (S.I. and J.A.T.), and the Japan Society for the Promotion of Science (K.H.). R.S.L. and I.G.M. acknowledge support from the Oregon Institute of Occupational Health Sciences at Oregon Health & Science University via funds from the Division of Consumer and Business Services of the State of Oregon (ORS 656.630). X-ray diffraction data were collected at the Stanford Synchrotron Radiation Laboratory (SSRL), supported by the Department of Energy (DOE) and NIH National Center for Research Resources, and at the Advanced Light Source, supported by NIH project ALS-ENABLE (P30 GM124169) and the Integrated Diffraction Analysis Technologies program of the US DOE Office of Biological and Environmental Research. An INCITE program award provided computer time to I.I., who also used the Oak Ridge Leadership Computing Facility, which is a DOE Office of Science User Facility supported under Contract DE-AC05-00OR22725. Figure panels 2b and 2f were created in BioRender (www.Biorender.com).

Competing interests

I.G.M. and R.S.L. are listed as inventors on a patent application pertaining to OGG1 activators (including F51) filed by OHSU. All other authors declare no competing interests.

Additional information

Supplementary information The online version contains supplementary material available at https://doi.org/10.1038/s41467-026-75471-1.

Correspondence and requests for materials should be addressed to Aleem Syed, Ivaylo Ivanov or John A. Tainer.

Peer review information *Nature Communications* thanks the anonymous reviewer(s) for their contribution to the peer review of this work. A peer review file is available.

Reprints and permissions information is available at http://www.nature.com/reprints

Publisher's note Springer Nature remains neutral with regard to jurisdictional claims in published maps and institutional affiliations.

Open Access This article is licensed under a Creative Commons Attribution-NonCommercial-NoDerivatives 4.0 International License, which permits any non-commercial use, sharing, distribution and reproduction in any medium or format, as long as you give appropriate credit to the original author(s) and the source, provide a link to the Creative Commons licence, and indicate if you modified the licensed material. You do not have permission under this licence to share adapted material derived from this article or parts of it. The images or other third party material in this article are included in the article's Creative Commons licence, unless indicated otherwise in a credit line to the material. If material is not included in the article's Creative Commons licence and your intended use is not permitted by statutory regulation or exceeds the permitted use, you will need to obtain permission directly from the copyright holder. To view a copy of this licence, visit http://creativecommons.org/licenses/by-nc-nd/4.0/.

© The Author(s) 2026

[1]Department of Molecular and Cellular Oncology, Department of Cancer Biology, The University of Texas MD Anderson Cancer Center, Houston, TX, USA. [2]Division of Radiation and Genome Instability, Department of Radiation Oncology, Dana-Farber Cancer Institute, Harvard Medical School, Boston, MA, USA. [3]Department of Chemistry, Georgia State University, Atlanta, GA, USA. [4]The Skaggs Institute for Chemical Biology and Department of Molecular Biology, The Scripps Research Institute, La Jolla, CA, USA. [5]Oregon Institute of Occupational Health Sciences, Oregon Health & Science University, Portland, OR, USA. [6]Graduate School of Engineering Science, Osaka University, Osaka, Japan. [7]Biological Systems and Engineering, Lawrence Berkeley National Lab, Berkeley, CA, USA. [8]Department of Biological Sciences, University at Albany-State University of New York, Albany, NY, USA. [9]Frontiers of Innovative Research in Science and Technology, Konan University, Kobe, Hyogo, Japan. [10]Department of Molecular and Medical Genetics, Oregon Health & Science University, Portland, OR, USA. [11]Life Sciences Division, Lawrence Berkeley National Laboratory, Berkeley, CA, USA. [12]These authors contributed equally: Aleem Syed, Leonardo F. Serafim. [19]Deceased: Clifford D. Mol. [20]Deceased: Kenichi Hitomi. ✉e-mail: aleem_syed@dfci.harvard.edu; iivanov@gsu.edu; jtainer@mdanderson.org